Evaluating MJO Event Initiation and Decay in the Skeleton Model using an RMM-like Index

Justin P. Stachnik[*1,2], Duane E. Waliser[1, 2], Andrew J. Majda[3], Samuel N. Stechmann[4], and Sulian Thual[3]

1. Joint Institute for Regional Earth System Science and Engineering, University of California, Los Angeles, Los Angeles, CA, USA.

2. Jet Propulsion Laboratory, California Institute of Technology, Pasadena, CA, USA.

3. Department of Mathematics and Center for Atmosphere–Ocean Science, Courant Institute, New York University, New York, NY, USA.

4. Department of Mathematics and Department of Atmospheric and Oceanic Sciences, University of Wisconsin–Madison, Madison, WI, USA.

Revised 28 September 2015

to Journal of Geophysical Research-Atmospheres

[*] Corresponding author: Justin P. Stachnik, Jet Propulsion Laboratory, 4800 Oak Grove Drive, M/S 233-304, Pasadena, CA 91109, USA. (Justin.P.Stachnik@jpl.nasa.gov)

Key Points

- An RMM-like index was created for the skeleton model that mimics observations
- Stochasticity helps improve MJO initiation and termination event statistics
- The skeleton model produces more realistic MJOs when forced with observed SSTs

Abstract

The Madden-Julian oscillation (MJO) skeleton model is a low-order dynamic model that is capable of simulating many of the observed features of the MJO. This study develops a model-based "MJO" index that is similar to the well-known real-time multivariate MJO (RMM) index to better facilitate comparison between the skeleton model and observational data. Multivariate and univariate empirical orthogonal function (EOF) analyses were performed on the convective heating and zonal wind data taken from the skeleton model for simulations forced with an idealized warm pool and observed sea surface temperatures (SSTs). The leading EOF modes indicated a wavenumber-1 convectively-coupled circulation anomaly with zonal asymmetries that closely resembled the observed RMM EOFs, especially when the model was forced with observed SSTs. The RMM-like index was used to compute an MJO climatology and document the occurrence of primary, continuing, and terminating MJO events in the skeleton model. The overall amount of MJO activity and event lengths compared reasonably well to observations for such a simple model. Attempts at reconciling the observed geographic distribution of individual MJO initiation and termination events were not successful for the stochastic simulations, though stochasticity is necessary in order to produce composite MJOs that initiate and decay with time scales similar to observations. Finally, analysis indicates that the existence of slow moving, eastward travelling waves with higher wavenumbers ($k \approx 12$) embedded within the large-scale flow often precedes MJO termination in the skeleton model.

1. Introduction

Intraseasonal variability of the tropical atmosphere is dominated by an eastward propagating equatorial mode known as the Madden-Julian oscillation (MJO), appropriately named after its initial discoverers [*Madden and Julian*, 1971; 1972]. The MJO represents a convectively-coupled mode of cloud and circulation anomalies on the planetary scale (i.e., wavenumbers 1-3) with an oscillation frequency of roughly 30-60 days [*Madden and Julian*, 1994; *Zhang*, 2005]. Deep convection associated with an MJO event generally appears as a broad envelope of cloud and precipitation anomalies that most commonly begins over the western or central Indian Ocean [e.g., *Matthews*, 2008; *Straub*, 2013] and propagates eastward at ~5 m s^{-1} until eventually terminating over the maritime continent or the central Pacific [e.g., *Stachnik et al.*, 2015]. The MJO directly impacts local weather and tropical climate and has also been shown to have far reaching dynamical effects including modifying the global monsoons [*Lau and Chan*, 1986; *Goswami and Ajaya Mohan*, 2001; *Matthews*, 2004; *Wheeler and Hendon*, 2004], genesis and intensification of tropical cyclones [*Maloney and Hartmann*, 2000; *Jiang et al.*, 2012], mid-latitude weather anomalies [*Higgins et al.*, 2000; *Bond and Vecchi*, 2003; *Guan et al.*, 2012], and may impact the onset of El Niño-Southern Oscillation (ENSO) events [e.g., *Lau and Waliser*, 2005].

Despite its global importance, successfully simulating the MJO remains a challenge in most global climate and weather forecast models [e.g., *Slingo et al.*, 1996, *Waliser et al.*, 1999, *Zhang et al.*, 2006; *Hung et al.*, 2013; *Jiang et al.*, 2015]. Global climate models (GCMs) generally struggle with initiating MJO events and often simulate weaker eastward propagation than observed in nature. Models with more realistic MJOs usually tune specific model parameters including estimates of air-sea coupling, the sensitivity of parameterized convection to

atmospheric moisture, or increase deep convection entrainment rates in order to delay convection (among others), which often comes at the sacrifice of a larger bias in the mean state [e.g., *Bechtold et al.*, 2008; *Hannah and Maloney*, 2011; *Benedict et al.*, 2013; *Klingaman and Woolnough*, 2014a; *Klingaman and Woolnough*, 2014b]. Recent advances using superparameterizations, in which a cloud resolving model is embedded within each GCM gridpoint, have demonstrated some success at improving simulations of the MJO [e.g., *Grabowski*, 2003; *Benedict and Randall*, 2009; *Pritchard and Bretherton*, 2014]. Nevertheless, these enhancements are inherently linked to a significant increase in the computational expense. Simple theoretical models, such as the multicloud model of *Khouider and Majda* [2006, 2007], have also been shown to improve simulated MJO variability when incorporated into aquaplanet and coarse-resolution GCMs [*Khouider et al.*, 2011; *Ajayamohan et al.*, 2013; *Deng et al.*, 2015]. Regardless, there is a pressing need for the refined development of computationally inexpensive, low-order models that are fully capable of simulating the large-scale, observed features of the MJO. Furthermore, incorporating these fundamental MJO dynamics into higher-order models may also help improve intraseasonal and medium-range weather forecasts.

The MJO skeleton model, developed by *Majda and Stechmann* [2009, 2011], is one such example of a low-order dynamical model that successfully simulates a number of salient features of the MJO including (1) an eastward propagation at ~5 m s^{-1}, (2) a unique dispersion relation with $\partial\omega/\partial k \approx 0$, and (3) a horizontal quadrupole vortex structure. Recent work by *Thual et al.* [2014] incorporated a stochastic element into the convective parameterization of the skeleton model and was able to further simulate (4) observed MJO event intermittency and (5) the organization of MJOs into circumnavigating events and wave trains as seen in nature [e.g., *Matthews*, 2008; *Yoneyama et al.*, 2013]. These MJO-like waves have also been positively

identified in observational data by *Stechmann and Majda* [2015] and *Ogrosky and Stechmann* [2015] using a new index that projects reanalysis data onto the theoretical linear solutions of the MJO obtained from the skeleton model (i.e., the amplitudes of the Kelvin and equatorial Rossby wave structures, moisture anomalies, and amplitude of convective heating). While the above index is proficient at isolating the observed MJO signal without the use of time filtering or empirical orthogonal functions (EOFs), its use should be supplemented by more common MJO metrics in order to better facilitate comparisons with higher-order GCMs and operational weather forecast models.

This work intends to evaluate and build a complementary index for the MJO skeleton model based on the widely-used real-time multivariate MJO (RMM) index of *Wheeler and Hendon* [2004]. The RMM index has experienced tremendous popularity over the last decade and there are a large number of studies compositing MJO data by RMM phase that permit a more direct comparison between the skeleton model and observations or GCMs. Moreover, defining an RMM-like index for the skeleton model provides the opportunity to evaluate higher-order features of the model solutions in a framework consistent with observations including MJO event climatology and the precursor conditions associated with the initiation and termination of MJO events.

This article is organized as follows. Section 2 gives a brief overview of the skeleton model in addition to the methods used to derive the RMM-like index. We extend the recent work by *Ogrosky and Stechmann* [2015] and run the model using either an idealized warm pool or a more realistic background state based on observed sea surface temperatures (SSTs). Comparisons of the fundamental MJO structures in the model are evaluated using the RMM-like framework and presented in section 3. We also evaluate the overall level of MJO activity in the

113 model along with several applications that include a comparison to the observed MJO event
114 climatology and identification of precursor conditions potentially responsible for MJO
115 termination following *Stachnik et al.* [2015]. Finally, section 4 closes with a summary and
116 discussion of key results while identifying avenues for continued and potential future work.
117
118 **2. Data and Methods**
119 *2.1. The Skeleton Model*
120 The MJO skeleton model [*Majda and Stechmann*, 2009, 2011] is a low-order, nonlinear
121 oscillator designed to qualitatively reproduce the main features of tropical atmospheric dynamics
122 at intraseasonal time and planetary scales. The skeleton model is unique in that the large-scale
123 waves are assumed to arise through neutrally stable interactions involving convectively-coupled
124 waves at the synoptic and mesoscale that are driven by planetary scale moisture anomalies
125 instead of instabilities that occur on the planetary scale. Strictly speaking, the basic model
126 premise assumes that the instabilities and damping take place on the synoptic or mesoscale, the
127 details of which are unimportant for the resulting convective heating that drives the large-scale
128 circulation anomalies at the planetary scale.
129 Consequently, the skeleton model comprises a simple Matsuno-Gill type model of the
130 equatorial primitive shallow water equations, without damping, to sufficiently represent the
131 planetary scale, dry dynamics (Equations 1-4). In addition, there are two evolution equations that
132 describe the time tendencies for the amplitude of the convective heating wave envelope and
133 lower tropospheric moisture anomalies, respectively (Equations 5-6). Given that observations of
134 the MJO often demonstrate positive low-level moisture anomalies preceding and in quadrature to
135 regions of deep convection [e.g., *Hendon and Salby*, 1994; *Myers and Waliser*, 2003], the

skeleton model parameterizes the time tendency of the convective envelope amplitude (a) as a function of lower tropospheric moisture anomalies (q). This relationship is signified by the nonlinear amplitude equation in the following set (Equation 7). The model equations in non-dimension units are thus

$$\frac{\partial u}{\partial t} - yv = -\frac{\partial p}{\partial x} \quad (1)$$

$$yu = -\frac{\partial p}{\partial y} \quad (2)$$

$$0 = -\frac{\partial p}{\partial z} + \theta \quad (3)$$

$$\frac{\partial u}{\partial x} + \frac{\partial v}{\partial y} + \frac{\partial w}{\partial z} = 0 \quad (4)$$

$$\frac{\partial \theta}{\partial t} + w = \bar{H}a - s^{\theta} \quad (5)$$

$$\frac{\partial q}{\partial t} - \bar{Q}w = -\bar{H}a + s^{q} \quad (6)$$

$$\frac{\partial a}{\partial t} = \Gamma q a, \quad (7)$$

where u, v, and w represent the zonal, meridional, and vertical velocities, respectively, p is pressure, and θ is potential temperature. $\bar{H}$ and $\bar{Q}$ are constants that scale the heating rate and approximate the background vertical moisture gradient, respectively. The quantity Γ is a positive proportionality constant. Finally, s^q and s^θ represent external radiative cooling and moistening terms that can be used to force the model. It should be noted that all variables, with the exception of a, are anomalies from a radiative-convective equilibrium state.

We use the simplest version of the skeleton model herein, where the above equations are reduced to a single dimension by horizontally and vertically truncating to retain only the first meridional Hermite function and vertical baroclinic mode. The effect of the meridional truncation is to maintain an equatorially symmetric heating structure that excites only Kelvin

waves and the first equatorially symmetric Rossby waves. Details of the truncations, along with the equations for the model solutions and their reconstructed variables, are provided in *Majda and Stechmann* [2009, 2011].

Recently, *Thual et al.* [2014] modified the nonlinear term *qa* in the convective parameterization (Equation 7) to include a stochastic birth-death process to better account for the effects of synoptic and mesoscale processes that introduce significant irregularity to the MJO. Specifically, the amplitude of the convective envelope was replaced by a random variable, *a*, that evolves according to

$$a = \Delta a \eta, \qquad (8)$$

where Δa is a fixed step and η is a non-negative integer. The probability (P) of any given value η is prescribed by the master equation

$$\frac{\partial P(\eta)}{\partial t} = [\lambda(\eta - 1)P(\eta - 1) - \lambda(\eta)P(\eta)] + [\mu(\eta + 1)P(\eta + 1) - \mu(\eta)P(\eta)], \qquad (9)$$

where λ and μ are the upward and downward transition rates, respectively. It should be noted that these transitions are small and the parameters have been carefully chosen such that the long-term average of the stochastic model solutions recovers the dynamics of the original deterministic model. Additional details regarding the stochastic version of the skeleton model are provided in *Thual et al.* [2014].

This study continues to apply the previous condition where the external sources of cooling and moistening are set equal (i.e., $s^q = s^\theta$), which conserves the vertically integrated moist static energy. This balance condition was used for both a horizontally homogeneous and idealized warm pool state in *Majda and Stechmann* [2009, 2011] and *Thual et al.* [2014], where the latter is shown by a simple cosine pattern in Figure 1a with its maximum amplitude shifted towards the longitudes where it is actually observed. Furthermore, the zonal average of the

external terms must be equal (i.e., $\overline{s^q} = \overline{s^\theta}$) in order for a steady-state solution to exist without damping in the above model [e.g., *Majda and Klein*, 2003]. In the interest of producing the best possible comparison with the observed RMM index, we also perform several new simulations using the National Oceanic and Atmospheric Administration (NOAA) Optimum Interpolation (OI) version 2 (v2) SSTs [*Reynolds et al.*, 2002] in order to provide a more realistic estimate of the zonal variability of the external forcing terms used in the model simulations. While the above approach is far simpler than using observed estimates of diabatic heating, convective heating, and latent heat fluxes to force the skeleton model [*Ogrosky and Stechmann*, 2015], it is nevertheless a meaningful assumption that zonal variations in moisture anomalies, radiative cooling, and convection arise primarily from the distribution of SSTs, particularly for a long-term climatology as considered in this study.

The annual average NOAA OI SSTs v2 (1971-2000) were meridionally averaged from 10°S-10°N and regridded to match the relatively coarse horizontal resolution of the skeleton model (625 km). A Poisson relaxation was also performed to interpolate over missing data (i.e., land) and the resulting zonal profile was smoothed such that it only retains contributions from the first eight Fourier modes (Figure 1b). Overall, the observed SSTs closely match the shape of the idealized warm pool, especially over the Maritime Continent and Pacific Ocean (120°E-120°W). Most notably, there is a secondary maximum in the observed SSTs over the Atlantic Ocean (60°W-0°E) and a slightly weaker zonal gradient over the Indian Ocean (60°E-120°E) than otherwise present in the idealized warm pool case. The effect of these differences on the MJO-like waves in the skeleton model will be further explored in section 3.

2.2. Defining an RMM-like Index

As previously mentioned, *Stechmann and Majda* [2015] developed an MJO skeleton index that successfully identified the MJO in observational data by projecting reanalysis onto the MJO modes obtained from the skeleton model when using a uniform background state [i.e., $s^q(x) = s^\theta(x) = \overline{s^\theta}$]. Thus, rather than an empirical basis function like the RMM indices, this index uses a theoretically based basis function obtained from the model. This analysis was extended in *Ogrosky and Stechmann* [2015] to a case with zonally varying forcing where $s^q(x) \neq s^\theta(x)$, which again summarizes the information from all MJO wavenumbers into a single quantity. While the MJO skeleton index has several advantages including not requiring any time-filtering nor the use of EOF analysis, its potential for comparison to previous work is mostly limited due to the relative newness of this index combined with a change in the means of obtaining the basis function.

In the present work, we develop an MJO index for the skeleton model that to first order contains many similarities to the RMM index of *Wheeler and Hendon* [2004]. Although there are many other indices that are currently used to identify the MJO including wavenumber-frequency filtering [e.g., *Wheeler et al.*, 2000], lower-tropospheric wind [e.g., *Maloney and Hartmann*, 1998], upper-troposphere divergence and velocity potential [e.g., *Chen and Del Genio*, 2009; *Ventrice et al.*, 2013], or time-filtered outgoing longwave radiation (OLR) and cloudiness datasets [e.g., *Hendon and Salby*, 1994; *Matthews*, 2000; *Matthews*, 2008; *Kiladis et al.*, 2014], the choice of the RMM index is particularly appropriate here given the fact that the RMM index is primarily sensitive to wavenumber-1 modes, planetary scale circulation anomalies, and a baroclinic structure [e.g., *Straub*, 2013] that are likely to be reproduced by the skeleton model given its focus on these scales.

The RMM is a combined index of cloudiness and circulation anomalies based on observed OLR and lower- and upper-tropospheric zonal winds taken from reanalysis data (U850 and U200, respectively). Accordingly, we must first decide what model variables are most appropriate to use as observational proxies when creating an RMM-like index from the skeleton model. The following analysis uses the zonal wind from the skeleton model as a direct substitute for the lower-tropospheric wind, whereas the convective (latent) heating variable $\overline{Ha}$ is used as a proxy for the observed OLR. *Stechmann and Ogrosky* [2014] showed that variations in the total diabatic heating (i.e., $\overline{Ha} - s^{\theta}$) were directly proportional to OLR in the tropics, especially when averaged for long time periods (i.e., multiple years or decades) as done in our analysis. As such, positive $\overline{Ha}$ anomalies (enhanced heating) can thus be thought to have the same physical interpretation as negative OLR anomalies (enhanced cloudiness and deep convection) in our index.

Although the RMM index uses three variables (OLR, U850, and U200), the choice of a bivariate index does not preclude a meaningful comparison of the skeleton model to observations. *Straub* [2013] calculated time series of the RMM principal components using a method identical to *Wheeler and Hendon* [2004] with additional experiments involving data withholding. *Straub* [2013] found that the bivariate correlations between the full RMM index and RMM indices calculated without U850 (i.e., OLR and U200 only) or U200 (i.e., OLR and U850) were 0.95 and 0.94 for the entire 1979-2010 period, respectively. Furthermore, time series constructed from a univariate analysis when considering only lower- or upper-troposphere zonal winds had correlation values in excess of 0.9 with the full RMM. Consequently, the RMM index is largely dependent on the circulation component alone and using a single-level for the zonal wind as done here should be sufficient for the detection and monitoring of planetary scale MJOs.

Following *Wheeler and Hendon* [2004], daily anomalies of the skeleton model variables were initially calculated by removing the long-term mean and first three harmonics of the annual cycle. It should be noted that while *Wheeler and Hendon* [2004] considered global data between 15°S-15°N, the skeleton model analysis is restricted to data at the equator since the initial truncation only retains the first meridional mode (i.e., no asymmetric modes). *Wheeler and Hendon* [2004] continue to remove longer-term variability by subtracting the component linearly related to a measure of ENSO SSTs and further subtract a 120-day mean of the previous 120 days to remove any additional aspects of interannual or decadal variability and long-term trends. Since the skeleton model does not account for ENSO physics and variability nor contains any time-dependent SSTs (recall, s^q and s^θ are fixed), we choose to instead time filter the daily anomalies using a 20-100 day Lanczos filter with 201 weights in order to better isolate the intraseasonal signal in the model following *Matthews* [2008]. Each variable in the time-filtered dataset is normalized by its global variance to ensure equal contributions to the combined EOF analysis, again using the methods documented in *Wheeler and Hendon* [2004]. Both univariate and multivariate EOF analyses were performed on the convective heating and zonal wind data taken from the skeleton model simulations. The filtered model data were then projected onto the leading two EOF modes to calculate the model principal components. Finally, the principal components from each simulation and corresponding EOF analysis were normalized by their standard deviation such that a value of unity represents anomalies of one standard deviation from the mean.

We refer to the RMM-like index for the model simulations as the skeleton multivariate MJO index (SMM) as we only briefly consider those cases using a univariate analysis. Likewise, the principal components from the skeleton model data are termed SMM1 and SMM2 and are

assigned their order based on which of the two leading EOFs most closely resembles the longitudinal structures of the observed RMM index shown in *Wheeler and Hendon* [2004]. The values of SMM1 and SMM2 can therefore be visualized in a 2-dimensional phase space similar to the RMM index with significant MJO activity defined as an SMM amplitude greater than or equal to one with eastward propagation indicated by a counter-clockwise rotation of the daily amplitudes in the corresponding phase space.

3. Results

The following analysis presents a comparison of the skeleton model simulations with either an idealized warm pool or the truncated, observed SSTs using the model set-up and framework established by *Thual et al.* [2014]. The default parameters and model constants for all simulations were also taken from *Thual et al.* [2014], with the sole exception that the zonal average of the radiative cooling term, $\overline{s^{\theta}(x)}$, is set equal to 1.0 K day^{-1} and 1.33 K day^{-1} for the idealized warm pool and observed SST cases, respectively. Although the skeleton model has recently been amended to include a seasonally migrating warm pool and multiple meridional modes [*Thual et al.*, 2015], in addition to a refined vertical structure [*Thual and Majda*, 2015], we restrict our initial discussion to the stochastic and deterministic model simulations using the idealized and observed, annual average SSTs.

3.1. Climatology and Variance of Simulations using Idealized and Observed Forcing

Time-longitude series of the anomalous 20-100 day filtered skeleton model variables ($\bar{H}a$, u, and q) are shown in Figure 2 for a representative 600 day period for the simulations using the idealized warm pool and truncated, observed SSTs (Case-WP and Case-SST8N,

294 respectively). In both cases, there appear to be several instances of eastward propagating, MJO-
295 like waves that travel at approximately 5-6 m s^{-1} throughout the domain. These waves are evident
296 throughout the entire period for Case-WP in the zonal wind (Figure 2b) with coherent eastward
297 propagating structures not appearing until after day 38200 for Case-SST8N (Figure 2e).
298 Although specific MJO events should not be directly compared between the two simulations,
299 Case-SST8N displays greater variance in the convective heating over the western Indian Ocean
300 (i.e., 60-90°E) and a stronger mean convective heating over the tropical Atlantic (60°W-0°E)
301 than identified for Case-WP (cf. Figures 2a and 2d). These areas of enhanced heating agree
302 exceedingly well with *Ogrosky and Stechmann* [2015], who calculated observed $\bar{H}a$ values from
303 precipitation data using the Global Precipitation Climatology Project (GPCP) [*Huffman et al.*,
304 2012] and similar model quantities from simulations forced with observed atmospheric OLR and
305 latent heat fluxes derived from reanalysis data [Figure 13 in *Ogrosky and Stechmann*, 2015].
306 Power spectra of the reconstructed convective heating and zonal wind as a function of the
307 zonal wavenumber (k) and frequency (ω) are shown in Figure 3 for a 34 year period from each
308 model simulation. Both Case-WP and Case-SST8N demonstrate significant power in the MJO
309 range (i.e., $1 \leq k \leq 5$ and $1/90 \leq \omega \leq 1/30$ cpd) with the peak power stretching along a band with
310 $\partial\omega/\partial k \approx 0$, an auspicious and recurring feature of the skeleton model [*Thual et al.*, 2014]. The
311 peak power in each case is also near the dispersion curves for the linear solutions from the
312 skeleton model (the black circles in Figure 3). As in *Waliser et al.* [2009], the breadth of the peak
313 in frequency and wavenumber for the convective heating (i.e., a proxy for precipitation) relative
314 to zonal wind is captured by the skeleton model, though the convective heating power in the
315 MJO band is nearly constant with increasing wavenumber unlike in observations where the
316 precipitation power is largely confined to $1 \leq k \leq 3$. Generally, the convective heating and zonal

317 wind for Case-SST8N shows increased power near the dispersion curves of both the MJO and
318 moist Rossby modes, likely due to the slightly higher values of s^q and s^θ in this region (67.5°E)
319 and zonal mean when compared to the scenario with the idealized warm pool. The peak power
320 for the stochastic model simulations also occurs at slightly lower frequencies than the MJO-
321 mode dispersion curves, similar to *Thual et al.* [2014]. In addition, there are secondary peaks in
322 $\overline{Ha}$ and u at double and triple the MJO-mode frequencies, both of which are likely attributed to
323 the nonlinear qa term in the skeleton model.
324 Figure 4 shows the leading two structures from a univariate EOF analysis of the
325 convective heating and zonal wind for Case-WP. While the variance in convective heating, $\overline{Ha}$,
326 is centered over the longitudes with the maximum forcing for the idealized warm pool case
327 (Figure 1a), the EOF structures for the univariate analysis show significant noise due to the
328 presence of nonlinear terms and inclusion of stochastic effects (Figures 4a and 4b), even after
329 having already applied a 20-100 day filter. Furthermore, EOF1 and EOF2 only each explain
330 3.4% of the observed variance despite using a sufficiently long record. Although the skeleton
331 model is already computed on a relatively coarse grid (625 km or 5.625°) the stochastic
332 processes in the model occur at scales too small to identify recurring modes with the simple
333 global EOF analysis without additional smoothing first being applied to the model data. In fact,
334 each of the first eight modes explained approximately the same amount of variance over the
335 entire 340 years of simulation data, indicating that the first two EOFs are not unique (not shown).
336 Meanwhile, the leading structures from the univariate zonal wind analysis for Case-WP show a
337 highly symmetric wavenumber-1 pattern centered about the maximum of the idealized warm
338 pool with 31.3% of the variance explained by the leading two modes (Figures 4c and 4d). The
339 third and fourth EOF structures for Case-WP identify a wavenumber-2 circulation anomaly

centered about the warm pool maximum that explain an additional 16.2% of the combined variance (not shown).

The first two modes from the multivariate EOF analysis for Case-WP are shown in Figures 5a and 5b. The order of the leading EOFs has been switched to better facilitate comparisons with the observed EOF patterns from *Wheeler and Hendon* [2004], which are plotted for reference in Figures 5c and 5d. The EOF structures for the convective heating anomalies improve significantly when constrained by the variations in zonal wind for the combined analysis with a clear zonal wavenumber-1 pattern of enhanced heating and cooling (cf. Figures 4a-4b and Figures 5a-5b). Albeit, the previous improvement comes at the expense of a reduction in the total explained variance, which is only 16.7% for the combined EOF analysis. The heating EOFs have a maximum correlation coefficient of 0.70 and 0.68 with the observed *Wheeler and Hendon* [2004] OLR EOFs (Figures 5c and 5d) when calculated at all longitudes in order to account for any longitudinal displacement of the convective features in the model (Table 1). The zonal wind structures in the multivariate analysis are nearly identical to the univariate patterns, suggesting that the combined index is far more sensitive to the circulation component alone as is the case in observations [e.g., *Straub,* 2013]. The multivariate circulation modes generally mimic the structures in the observed *Wheeler and Hendon* [2004] EOFs with a maximum correlation of 0.83 and 0.72 (Table 1), though the observed EOF patterns contain more asymmetry and explain a higher percent of the total variance (25.0%) than Case-WP from the skeleton model. Regardless, it is impressive the skeleton model is able to reproduce the salient features of the observed RMM index considering the many simplifications in the model and use of an idealized warm pool in lieu of observed SSTs.

The equivalent multivariate EOF modes for the skeleton model simulation using the truncated, observed SSTs (Case-SST8N) are shown in Figures 6a and 6b. Compared to Case-WP, the addition of the observed s^q and s^θ increases the asymmetry in the convective heating and zonal wind structures and better matches the observed *Wheeler and Hendon* [2004] EOFs (Figures 6c and 6d). As such, the maximum correlation coefficient between the model and observed EOFs increases from 0.70 and 0.68 (Case-WP) to 0.89 and 0.80 (Case-SST8N) for the convective heating variable (Table 1). Likewise, the correlations for the circulation anomalies increase from 0.83 and 0.72 to an incredible 0.98 and 0.94 for Case-WP and Case-SST8N, respectively (Table 1) As in Case-WP, the model EOF structures are in quadrature with the maximum cross-correlation (i.e., between the corresponding principal components) for Case-SST8N at 9 days (Figure 7), consistent with observations and suggesting an overall MJO oscillation frequency of ~40 days.

The peak positive values in zonal wind for the Case-SST8N multivariate EOFs are located about 30-40° east of where the maxima occur in observations (Figure 6). The combined EOFs also explain 15.7% of the total variance, which is slightly lower than for Case-WP. Nevertheless, the multivariate EOFs bear a striking resemblance to the observed EOF patterns from the RMM index, with maximum correlations of 0.98 and 0.94 for the circulation component and 0.89 and 0.80 for the convection anomalies (Table 1). As such, we therefore choose to also project the model data directly onto the *Wheeler and Hendon* [2004] EOFs when deriving various forms of the model principal components (i.e., hybrid SMM1 and SMM2 values that depend on both the model and observations) in order to directly evaluate how well the skeleton model is able to reproduce observed MJO event statistics using the RMM framework. The use of a reference set of EOFs for calculating the model principal components also provides

385 a valuable standard and better facilitates comparison of MJO climatology statistics from different
386 model simulations using varying parameters or forcing data.
387
388 *3.2. Identifying MJO Events in the Skeleton Model*
389 Having already developed an RMM-like index that is similar to observations, we now
390 turn our attention to applications of the SMM index, including the identification of MJO events
391 in the skeleton model. Similarly, we also document the sensitivities of using the model-derived
392 univariate and multivariate EOFs, in addition to the *Wheeler and Hendon* [2004] observed
393 multivariate EOFs for the resulting MJO event climatology.
394 This study uses the common practice of one standard deviation (i.e., a combined
395 amplitude greater than or equal to unity) as a lower threshold for defining the presence of a
396 strong MJO. In addition, we employ the technique used in *Stachnik et al.* [2015], where the daily
397 values of RMM1 and RMM2 must contain nearly continual counter-clockwise rotation (i.e.,
398 eastward propagation) in the 2-dimensional phase space of *Wheeler and Hendon* [2004]. We also
399 require that a simulated MJO "event" pass through at least four phases of the SMM index.
400 Two examples of simulated MJO-like waves are shown in Figure 8 for Case-WP. For
401 each event, the SMM index was calculated by projecting the skeleton model data onto the
402 multivariate, observed *Wheeler and Hendon* [2004] EOFs. Using the above definition, a primary
403 MJO event initiates on day 30564 and day 32665 for the periods in Figures 8a and 8b and are
404 noted with a gray circle for the first days when the combined SMM amplitude grows above 1.0
405 along the far eastern edge of the RMM phase 8 domain and western region of RMM phase 6,
406 respectively. The MJO event in Figure 8a begins to propagate eastward through two phases
407 (RMM phase 8 and phase 1) before being identified as a continuing MJO event (in contrast to

primary events that develop from inactive conditions) provided that it propagate through four additional phases as is highlighted in blue. These conditions are met again as the MJO moves into the RMM phase 3 and phase 4 domains, each counting as a separate continuing event with the subsequent paths colored in green and orange, respectively. For simplicity, only the first day of the continuing events are shown in Figure 8b, with a special circumnavigating event or wave train MJO denoted in gold for RMM phase 6 once the MJO-like wave has successfully propagated around all longitudes. As such, the initiation of each primary MJO may contain multiple continuing events, especially for very long-lasting MJOs.

Termination events occur when the SMM amplitude decays below unity for an extended period of time or demonstrates significant westward propagation. Examples of MJO termination events are shown in RMM phase 7 and phase 1 for Figures 8a and 8b, respectively. Overall, the event histories are much smoother than in observations [e.g., Figure 1 in *Stachnik et al.*, 2015], even when projecting the model data directly onto the *Wheeler and Hendon* [2004] EOFs. This artifact is partially by design, as the skeleton model was specifically developed for intraseasonal and planetary oscillations. The use of a band-pass filter on the model data, while able to better isolate the intraseasonal signal, lacks the same day-to-day noise and high frequency variability originating from convectively coupled equatorial waves and other disturbances that are capable of projecting upon the RMM index in nature [e.g., *Roundy et al.*, 2009]. Additional details and sensitivities of the search algorithm are described in *Stachnik et al.* [2015].

Table 2 lists the number of MJO events from 34 years of observations (1979-2012) using the historical RMM index and the mean and 95% confidence intervals for an equivalent 34 year period derived from 680 years of skeleton model data using an idealized warm pool (Case-WP). Overall, the number of simulated MJO events is in fairly good agreement with observations

when one considers the highly idealized form of the model and the lack of model tuning relative to this metric. In detail, for all methods of calculating the SMM index (i.e., univariate and multivariate model EOFs in addition to the multivariate observed EOFs) the number of primary MJOs is less than observations with a range 89.3-97.7 events for the skeleton model compared to 154 events in observations. The uncertainty estimates for primary MJO events are fairly small, with a limited range of 3.6-4.8% relative to the mean number of events. With the exception of the univariate zonal wind EOF analysis, the mean number of continuing events exceeds observations, though the observed number falls within the 95% confidence intervals in each case. Similarly, all of the Case-WP scenarios contain approximately 40-60% more circumnavigating events than actually occur. Finally, the number of terminating events is identical to the primary MJOs, as all events that initiate must eventually come to an end in the skeleton model.

The decrease in the number of separate MJO events in the skeleton model while maintaining a nearly equal or slightly greater number of continuing and circumnavigating events implies that the average MJO event length (i.e., the number of days between event initiation and termination) should be higher in the model than observations. This presumption is correct, with a mean model event length of about 40 days for all realizations from Case-WP in contrast to an approximate 35 day event length in observations (Table 2). Also, it is interesting to note that there is little overall sensitivity to the choice of EOFs when creating the model event climatology. Nevertheless, using the observed *Wheeler and Hendon* [2004] EOFs resulted in the most favorable comparison for primary MJOs with those seen in nature.

Similar results for the number of MJO events and average MJO event length are provided in Table 3 for the case using the truncated, observed SSTs (Case-SST8N). Once again, the number of primary MJOs is less than in observations, with only about 64% the number of

observed MJOs regardless of the choice in EOFs. Here, the percent increase in the number of continuing and circumnavigating events is higher than for Case-WP, with 443.5-477.9 continuing events and 33.4-36.6 circumnavigating MJOs in the skeleton model compared to 330 and 15 MJO events in observations, respectively. As a result, the average MJO event length for Case-SST8N is higher than the idealized warm pool simulation, with an average length of approximately 44 days.

The increase in the average MJO event length for the skeleton model simulations is somewhat deceptive, however, as further investigation revealed that the mean event length is primarily skewed by a smaller number of simulated events that have very long length. Figure 9 shows the cumulative probability distribution function of the observed (black) and modeled (blue) MJO event lengths for a representative 34 year simulation period using the truncated, observed SSTs. Approximately two-thirds of the observed events fall within 20-100 days with a slightly lower (~60%) percent of simulated MJOs from Case-SST8N in the same range (Figure 9). Furthermore, the shortest 40-50% of simulated MJO events in the stochastic version of the skeleton model match observations.

Moreover, the introduction of stochasticity in the model is critical for generating a more realistic MJO event climatology. Additional simulations using the deterministic version of the model with the idealized warm pool or observed SSTs (Case-WPdet and Case-SST8Ndet, respectively) showed about a 10% reduction in the number of primary MJOs compared to their corresponding stochastic simulation. The deterministic solutions also had an approximate 130% and 175% increase in the number of continuing events for Case-WPdet and Case-SST8Ndet, respectively (Table 4). The resulting average MJO event lengths for the deterministic solutions far exceeds observations, with Figure 9 indicating a significant positive bias for all MJO event

lengths for a representative 34 year period of Case-SST8Ndet (red). In fact, nearly 10% of the simulated MJOs last more than 150 days in this case.

3.3. Geographic Distribution of MJO Events in the Skeleton Model

Thus far, the use of real data SSTs in the skeleton model has been shown to produce more realistic multivariate EOF structures with higher correlation values that better match the observed *Wheeler and Hendon* [2004] RMM EOFs. Furthermore, those model simulations using observed forcing [*Ogrosky and Stechmann*, 2015] produce a more realistic geographic distribution of convective heating with an increase in $\bar{H}a$ variance over the locations where it is actually observed. Therefore, it becomes reasonable to wonder how zonal variations in the external forcing terms might alter the geographic distribution of MJO initiation and termination events in the skeleton model. Prior to applying this test for natural climate variability such as the modulated forcing due to ENSO or Indian Ocean dipole (IOD) SSTs, it is first necessary to determine whether the skeleton model can reproduce the observed geographic variability of MJO initiation and termination events using annual average SSTs.

Figure 10 shows the relative frequency of occurrence for primary, continuing, and terminating MJO events subset by RMM phase for 34 years of observations and similar periods of model data for Case-WP, Case-SST8N, and Case-SST8Ndet using the observed *Wheeler and Hendon* [2004] EOFs when calculating the model climatology. While the figures are similar to the 2-dimensional phase space diagrams from *Wheeler and Hendon* [2004], the plots indicate the percent likelihood of each MJO event type visualized in a radial-frequency domain. On average, observed MJO events are most likely to initiate over the Indian Ocean (RMM phase 2) and terminate over the Western Pacific or western hemisphere (RMM phase 6 and phase 8), as

500 evidenced in Figure 10a. Figure 10b shows an analogous distribution for a single 34 year period
501 for Case-WP. There is some suggestion that the simulated MJOs prefer to initiate in the RMM
502 phase 1 and phase 2 domains, with local termination maxima in RMM phase 8 and phase 5 (i.e.,
503 western hemisphere and exiting the Maritime Continent, respectively). Comparisons for Case-
504 SST8N (Figure 10c) are in less agreement, however, with a large termination peak located within
505 the RMM phase 3 domain that does not match observations. The deterministic model simulation
506 for this case (Case-SST8Ndet) is also different from observations with the simulated MJOs
507 becoming too regular and preferentially beginning and terminating in RMM phase 3 and phase 2,
508 respectively (Figure 10d).

509 To better determine whether or not the skeleton model is capable of reproducing the
510 observed MJO event climatology as a function of the large-scale forcing, we extend the previous
511 analysis to 680 years of model data, i.e., 20 independent samples of 34 year periods similar in
512 length to the observations. Figure 11 displays the mean event frequencies and 95% confidence
513 intervals as a function of RMM phase for the observations and five different model simulations.
514 In all panels, the uncertainty is calculated using a binomial proportion confidence interval that is
515 dependent on the pass and fail rates of the *N* events being assigned to a particular RMM phase
516 throughout the entire record. As such, the results are only statistically significant if the
517 confidence intervals do not overlap the reference line of 12.5%, i.e., the equal likelihood that an
518 MJO event will occur within any of the eight RMM phases.

519 Unfortunately, most of the frequencies in Figure 11a cannot be treated as statistically
520 significant or different from an equal chance due to the relatively large confidence intervals and
521 shorter historical record for observed MJOs. The skeleton model, however, is not constrained by
522 the lack of samples and can be run for extended periods. As a check, we perform the same

523 analysis on a special long-term stochastic simulation using a homogenous background (Case-
524 HG) where the principal components are calculated using the model's own multivariate EOFs,
525 while the other simulations use the observed *Wheeler and Hendon* [2004] EOFs. This situation
526 should be most likely to produce equal chance results for all RMM phases given the absence of
527 geographically varying forcing or data projection upon the observed EOFs and is successfully
528 recovered in Figure 11d. Only a few of the mean frequencies for Case-WP or Case-SST8N
529 (Figures 11b and 11c) demonstrate any statistical significance from an equal probability and the
530 peaks in the MJO event distributions do not necessarily match observations. It remains possible,
531 however, that the stochastic effects in the model act to dilute the geographic dependencies and
532 impacts of applying zonally varying forcing. The long-term climatology for Case-WPdet (Figure
533 11e) does show some features in common with the observed locations of MJO event initiation
534 that are statistically significant yet demonstrate little skill for the corresponding climatology of
535 termination events. The frequency distribution for Case-SST8Ndet (Figure 11f) produces the
536 largest differences from an equal chance, though those phases with distinguishable frequencies
537 do not match observations. As such, more work is needed to help separate the effects of
538 nonlinearity, stochasticity, and zonally-varying forcing upon where MJO events begin and decay
539 in the skeleton model. Similarly, the model may need to account for other factors such as
540 interactions with the extratropical circulation before making any firm conclusions regarding its
541 potential future use in studying natural climate variability and change.
542
543 *3.4. Composites and Precursors for MJO Initiation and Termination*
544 Figure 12 shows the composite RMM1-RMM2 indices associated with primary MJO
545 event initiation for all phases in observations and the corresponding SMM1-SMM2 histories

546 from a single 34 year period of skeleton model data for Case-WP, Case-SST8N, and Case-
547 SST8Ndet. The observed *Wheeler and Hendon* [2004] EOFs were used to calculate the principal
548 components in each model case and the day 0 (i.e., first day with combined amplitude greater
549 than 1.0) is noted with a circumscribed X in all panels.

550 In the observations and stochastic simulations, MJO initiation occurs rather quickly, with
551 a rapid increase in the combined amplitudes for the three days prior to the initiation event. The
552 observational composite shows continued growth for an additional 2-3 days with most phases
553 achieving a near constant value with only weak growth of the combined amplitude through the
554 following 12 days (Figure 12a). Meanwhile, the stochastic simulations share the same initial
555 growth (i.e., rapid intensification for 3 days prior to initiation) though continue to intensify
556 beyond observed values and reach a maximum SMM amplitude 5-6 days after the initiation of an
557 event (Figures 12b and 12c). Overall, the average root-mean-square error (RMSE) for all eight
558 phases is 0.27 and 0.23 amplitude units for Case-WP and Case-SST8N, respectively. The
559 initiation composite for the deterministic simulation follows the same trend as the observations
560 and stochastic runs although the SMM amplitude growth rates are much slower before and after
561 MJO initiation (Figure 12d). Consequently, the smaller changes in SMM amplitude for Case-
562 SST8Ndet result in the largest values of RMSE (0.29 amplitude units) and do not match the
563 observations as well at the stochastic simulations.

564 Analogous RMM and SMM composites are shown before and after the start of an MJO
565 termination event in Figure 13. Again, 2-3 days seems to be the relevant time scales for the
566 decay of an observed MJO event as the combined RMM amplitudes maintain nearly constant
567 values in the composite until approximately 3 days prior to the termination markers that indicate
568 the last day where the combined amplitude remains above unity (Figure 13a). Only RMM phase

2 termination events experience gradual decay, with the RMM amplitude weakening for about 7 days prior to termination [*Stachnik et al.*, 2015]. The composites for the stochastic model simulations attain stronger values of SMM amplitude 5-6 days prior to the eventual termination event than seen in observations (Figures 13b and 13c). The average RMSE values are 0.27 and 0.26 for Case-WP and Case-SST8N, respectively. As with initiation, the changes in SMM amplitude for Case-SST8Ndet occur more slowly are much smaller than actually observed (Figure 13d). However, the RMSE for the deterministic run is slightly smaller (0.24 amplitude units) given the pronounced pulsing in SMM amplitude prior to termination for the stochastic simulations during this period.

In order to identify possible mechanisms for MJO termination, Figure 14 shows the lag-longitude composites of the anomalous convective heating, moisture, and zonal wind at the equator from 340 years of MJO events that either continue or terminate in the RMM phase 6 region for Case-SST8N when using the observed *Wheeler and Hendon* [2004] EOFs. We focus on this domain given the fact that observed MJOs often terminate in region (e.g., Figure 10a). In addition, the RMM6 domain allows for a longer analysis of the upstream conditions prior to the termination event without the complication of circumnavigating the western hemisphere. All of the model variables have been time filtered to isolate the 20-100 day intraseasonal variability. Differences between the continuing and terminating events are shown in the bottom panel of each column along with stippling that indicates the presence of a statistically significant different mean associated with continuing and terminating MJOs.

To begin, the differences in the large-scale environmental conditions at positive lags (i.e., after the termination of an MJO event) are not nearly as pronounced as they are in observations [cf. Figure 4 in *Stachnik et al.*, 2015]. For example, the zonal wind maintains a wavenumber-1

592 type circulation anomaly after day 0 for the terminating cases in the skeleton model (Figure 14h)
593 with the main difference being a weaker amplitude than identified during positive lags for the
594 continuing events (Figure 14g). Conversely, the wavenumber-1 circulation anomaly decays
595 rapidly when compositing low-level zonal winds from reanalysis data for terminating MJO
596 events [Figure 4 in *Stachnik et al.*, 2015]. In addition, there is no single variable that seems to
597 best predict whether an MJO event will continue or terminate once entering the RMM phase 6
598 domain. Unlike in observations, significant differences between continuing and terminating
599 events occur in both the active and inactive phases of the MJO for the $\overline{Ha}$, q, and u anomalies.
600 These difference appear to manifest within MJO wave trains and are identifiable more than 30
601 days prior to the eventual continuing or terminating event. The above result is intriguing,
602 considering that the composite SMM indices in Figure 13 only suggest a weakening of the
603 SMM1-SMM2 amplitudes in the 5-6 days immediately prior to event termination. As such, it is
604 not immediately clear what sort of physical precursor conditions may be affecting MJO
605 termination in the skeleton model.
606 Figure 15 expands the above analysis to include composites and differences in
607 convergence and potential temperature for the 340 year period of continuing and terminating
608 MJOs. The rightmost column of Figure 15 shows the potential temperature composites for a
609 shorter, single 34 year period of skeleton model data. Once more, the differences in convergence
610 and potential temperature at positive lags for termination events is more closely related to
611 amplitude differences rather than a complete shutdown of the large-scale pattern. However, it is
612 interesting to note that there are a number of slow moving (~1 m s^{-1}), eastward propagating
613 waves embedded within the composite difference panels for the convergence and potential
614 temperature in Figures 14c, 14f, 15c, and 15f. These anomalies occur at relatively high

615 wavenumber ($k \approx$ 12-13) are even more pronounced in the termination composites for the shorter
616 34 year period (cf. Figures 15g and 15h). *Majda and Stechmann* [2011] also noted potential
617 interactions of dry Kelvin and Rossby modes during MJO termination for the skeleton model,
618 though the waves in our analysis travel much more slowly than these theoretical modes. Albeit
619 highly speculative, the previous results suggest that continuing MJO events may suppress the
620 development of eastward propagating waves. Alternatively, the emergence of dry Kelvin waves
621 in *Majda and Stechmann* [2011] or other higher wavenumber modes embedded within the large-
622 scale flow as seen here may interfere with the MJO dynamics and help lead to its future demise.
623 Finally, Figure 16 shows the distribution of zonal wind and moisture anomalies for
624 individual RMM phase 6 MJOs averaged over the local domain (120-160°E) at 10 days prior to
625 the continuing or terminating event for Case-SST8N. As is the case with observations in
626 *Stachnik et al.* [2015], there is appreciable overlap in the anomaly distributions for individual
627 continuing and terminating events despite containing a statistically significant different mean for
628 the time and longitudes displayed (e.g., Figure 14i). For example, individual continuing MJO
629 events may contain cooling and drying whereas terminating events may experience moistening
630 and warming (Figure 16b). Subsequently, there appears to be no one recurring or unique set-up
631 for MJO termination even in the relatively simple and low-order stochastic skeleton model.
632
633 **4. Summary and Discussion**
634 This study developed an RMM-like index for the deterministic and stochastic version of
635 the MJO skeleton model [*Majda and* Stechmann, 2009; 2011] using an approach similar to that
636 outlined in *Wheeler and Hendon* [2004]. Univariate and multivariate EOF analyses were
637 performed using convective heating and zonal wind data taken from the skeleton model

638 simulations forced with an idealized warm pool and observed SSTs. The simulations with the
639 observed SSTs (Case-SST8N) demonstrated a number of small improvements over the idealized
640 warm pool (Case-WP) and was consistent with the observationally-motivated skeleton model
641 simulations performed by *Ogrosky and Stechmann* [2015]. Moreover, the leading modes of the
642 multivariate EOF analysis from Case-SST8N had greater correlations than the corresponding
643 modes from Case-WP while also containing zonal asymmetries that more closely resembled the
644 observed *Wheeler and Hendon* [2004] RMM EOFs. Overall, the leading EOFs for the
645 multivariate analysis of Case-SST8N showed a wavenumber-1 convectively-coupled circulation
646 anomaly that explained 15.7% of the total variance. The skeleton multivariate MJO (SMM)
647 index also relied more heavily on the circulation component, as is the case in observations [e.g.,
648 *Straub*, 2013], given the lack of a well-defined univariate EOF mode for convective heating in
649 the model data. Correlation coefficients between the values of SMM1 and SMM2 derived from a
650 univariate zonal wind analysis (i.e., u only) and the full SMM index ($\overline{Ha}$ and u) were in excess
651 of 0.98 when considering 680 years of model data for both Case-WP and Case-SST8N.
652 A climatology of MJO events was performed using multiple forms of the SMM index for
653 the skeleton model. It was shown that the stochastic skeleton model produces a number of MJO
654 events that, for such a simple model, compares reasonably well with the observed number of
655 MJO events documented in *Stachnik et al.* [2015]. As such, the average MJO event length in the
656 model was approximately 40 days and 44 days for Case-WP and Case-SST8N, respectively,
657 which is only slightly higher than in observations (~35 days). Distributions of the average event
658 length revealed that the skeleton model does a good job of simulating the shortest 40-50% of
659 MJO events and that the average length is skewed by the occasional presence of very long MJOs
660 not seen in nature, suggesting that the stochastic parameters used in the model are well-tuned.

661 The existence of additional circumnavigating and long-lasting MJOs in the model is reasonable,
662 however, given the lack of damping on the planetary scale and the omission of other factors such
663 as enhanced friction over land surfaces that may help terminate observed events. The total
664 number of MJOs and corresponding event lengths were relatively insensitive to the choice of
665 EOFs (e.g., model univariate, multivariate, or the observed RMM patterns) used to calculate the
666 SMM index.

667 An initial attempt was made to quantity the geographic distributions of MJO event
668 initiation and termination based on the large-scale forcing. Whereas most of the model quantities
669 were relatively stable for shorter periods that mimicked the length of observations (34 years), the
670 frequencies of MJO initiation in a given RMM phase varied strongly over shorter time periods
671 and required a much longer record (680 years) for analysis. While the simulated climatology for
672 shorter periods may occasionally resemble observations, the long-term record for the stochastic
673 model simulations showed nearly equal chance for an MJO event to initiate or terminate in any
674 RMM phase despite the existence of zonal variations in the external radiative cooling and
675 moistening terms used to force the model. The deterministic solutions did show statistically
676 significant preferred regions of MJO initiation and termination for the long-term analysis, though
677 these features did not always match observations.

678 The previous finding presents a bit of conundrum, considering that using observed SSTs
679 to force the model results in a more realistic representation of the mean convective heating and
680 variance that is in agreement with *Ogrosky and Stechmann* [2015] while also producing
681 multivariate EOF structures that more closely resemble the observed RMM patterns taken from
682 *Wheeler and Hendon* [2004]. Despite this fact, the stochastic simulation using the observed SSTs
683 provided no improvement over the idealized warm pool case for accurately simulating the

observed geographic variability of MJO initiation and termination events. The effect of stochasticity here appears to distribute the start and finish of individual MJO events more equally throughout the domain while maintaining the overall amount of MJO activity in the model. The MJO events initiated and terminated in all RMM phases, albeit some phases were preferred for the deterministic model simulations that did not necessarily match observations.

While the basic model assumptions and observed, annual average SSTs may be sufficient to generate reasonable looking MJO dynamics, structures, variability, and number of events, additional factors beyond internal tropical variability and the climatological forcing may be required to produce realistic distributions of MJO initiation and decay events. For example, MJOs may initiate from any number of mechanisms including influences from higher latitudes such as cold air outbreaks and Rossby wave trains [e.g., *Hsu et al.*, 1990; *Matthews and Kiladis*, 1999; *Ray and Zhang*, 2010; *Wang et al.*, 2012] or topographic effects [e.g., *Hsu and Lee*, 2005], all of which have geographic variability that are not accounted for in the current version of the skeleton model. Future work will continue to evaluate long-term records of simulated MJO behavior from the skeleton model as a function of the shape and strength of the tropical warm pool in order to determine if the model is capable of identifying shifts in the location or lifetimes of MJO events as a function of ENSO [e.g., *Pohl and Matthews*, 2007] or Indian Ocean dipole (IOD) SSTs.

Including stochastic effect within the convective parameterization were also necessary for the model to produce more realistic estimates of the time scales for MJO event initiation and termination. The introduction of the stochastic parameterization better accounts for the random component of the growth and decay of unresolved synoptic and mesoscale convective processes that occur within the MJO envelope. These processes are needed here, and likely in nature, to

accelerate the time scales of initiation and decay that are otherwise too slow through the neutrally stable wave interactions and large-scale moisture depletion that occurs in the deterministic version of the skeleton model. In fact, almost every one of the stochastic model simulations produced a more realistic looking MJO initiation and termination composite with smaller RMSE values regardless of the choice of EOFs when calculating the principal components or background forcing when compared to its corresponding deterministic solution (not shown).

Finally, we examined the large-scale conditions associated with the termination of MJO events in the skeleton model over the RMM phase 6 domain. As previously reported through a visual analysis of MJO time series in *Majda and Stechmann* [2009, 2011] and *Thual at al.* [2014], the skeleton model produced MJO events that either stalled or experienced decay immediately upstream or directly over the warm pool maximum as observed in nature. However, it is important to note that these successes may not be for the correct physical reasons, as the observed MJO encounters a number of additional factors that may weaken it over this domain that are not accounted for in the skeleton model such as stronger diurnal cycles, topographic effects, and enhanced boundary layer friction over land. Moreover, our analysis of the precursor conditions associated with MJO decay in the skeleton model indicated that higher wavenumber ($k \approx$ 12-13) oscillations embedded within the large-scale flow could be important for MJO termination. Whether the development of these waves are either suppressed by continuing MJO events, or alternatively, the emergence of eastward propagating waves contribute towards MJO event termination remains unknown. Our future work plans to examine the wave power spectra associated with MJO termination events in observations and the skeleton model to better elucidate what mechanisms may be responsible for MJO initiation and decay.

Acknowledgments

The RMM index was obtained from the Australian Bureau of Meteorology website. The NOAA OI SST v2 data were provided by the NOAA/Office of Oceanic and Atmospheric Research (OAR)/Earth System Research Laboratory (ESRL) Physical Sciences Division (PSD) in Boulder, CO, USA, and obtained from their website at http://www.esrl.noaa.gov/psd/. Three anonymous reviewers provided helpful comments. Part of this research was carried out at the Jet Propulsion Laboratory, California Institute of Technology, under a contract with the National Aeronautics and Space Administration. This study was funded by the Office of Naval Research (ONR) award number N00014-12-1-0912.

740 **References**

741 Ajayamohan, R. S., B. Khouider, and A. J. Majda (2013), Realistic initiation and dynamics of the
742 Madden-Julian oscillation in a course resolution aquaplanet GCM, *Geophys. Res. Lett.*,
743 *40*, 1-6, doi:10.1002/2013GL058187.

744 Bechtold, P., M. Köhler, T. Jung, F. Doblas-Reyes, M. Leutbecher, M. J. Rodwell, F. Vitart, and
745 G. Balsamo (2008), Advances in simulating atmospheric variability with the ECMWF
746 model: From synoptic to decadal time-scales, *Q. J. Roy. Meteor. Soc.*. *134,* 1337–1351,
747 doi: 10.1002/qj.289.

748 Benedict, J. J., E. D. Maloney, A. H. Sobel, D. M. Frierson, and L. J. Donner (2013), Tropical
749 intraseasonal variability in version 3 of the GFDL atmosphere model, *J. Climate*, *26*,
750 426–449.

751 Benedict, J. J., and D. A. Randall (2009), Structure of the Madden–Julian oscillation in the
752 superparameterized CAM, *J. Atmos. Sci.*, *66*, 3277-3296.

753 Bond, N. A., and G. A. Vecchi (2003), The influence of the Madden–Julian oscillation on
754 precipitation in Oregon and Washington, *Wea. Forecasting*, *18*, 600-613.

755 Chen, Y.-H., and A. D. Del Genio (2009), Evaluation of tropical cloud regimes in observations
756 and a general circulation model, *Climate. Dyn.*, *32*, 355-369.

757 Deng, Q., B. Khouider, and A. J. Majda (2015), The MJO in a coarse-resolution GCM with a
758 stochastic multicloud parameterization, *J. Atmos. Sci.*, *72*, 55–74.

759 Goswami, B. N., and R. S. Ajaya Mohan (2001), Intraseasonal oscillations and interannual
760 variability of the Indian summer monsoon, *J. Climate*, *14*, 1180-1198.

761 Grabowski, W. W. (2003), MJO-like coherent structures: Sensitivity simulations using the cloud-
762 resolving convection parameterization (CRCP), *J. Atmos. Sci.*, *60*, 847-864.

763 Guan, B., D. E. Waliser, N. P. Molotch, E. J. Fetzer, and P. J. Neiman (2012), Does the Madden–
764 Julian oscillation influence wintertime atmospheric rivers and snowpack in the Sierra
765 Nevada?, *Mon. Wea. Rev.*, *140*, 325–342.
766 Hannah, W. M., and E. D. Maloney (2011), The role of moisture–convection feedbacks in
767 simulating the Madden–Julian oscillation, *J. Climate*, *24*, 2754–2770.
768 Hendon, H., H., and M. L. Salby (1994), The life cycle of the Madden–Julian oscillation, *J.*
769 *Atmos. Sci.*, *51*, 2225-2237.
770 Higgins, R. W., J.-K. E. Schemm, W. Shi, and A. Leetmaa (2000), Extreme precipitation events
771 in the western United States related to tropical forcing, *J. Climate*, *13*, 793-820.
772 Hsu, H.-H., B. J. Hoskins, and F.-F. Jin (1990) The 1985/86 intraseasonal oscillation and the role
773 of the extratropics, *J. Atmos. Sci.*, *47*, 823-839.
774 Hsu, H.-H., and M.-Y. Lee (2005): Topographic effects on the eastward propagation and
775 initiation of the Madden–Julian oscillation, *J. Climate*, *18*, 795–809.
776 Hung, M.-P., J.-L. Lin, W. Wang, D. Kim, T. Shinoda, and S. J. Weaver (2013), MJO and
777 convectively coupled equatorial waves simulated by CMIP5 climate models, *J. Climate*,
778 *26*, 6185-6214.
779 Huffman, G. J., R. F. Adler, D. T. Bolvin, and G. Gu (2009), Improving the global precipitation
780 record: GPCP version 2.1. *Geophys. Res. Lett.*, *36*, L17808, doi:10.1029/2009GL040000.
781 Jiang, X., et al. (2015), Vertical structure and physical processes of the Madden-Julian
782 oscillation: Exploring key model physics in climate simulations, *J. Geophys. Res. Atmos.*,
783 *120*, 4718–4748, doi:10.1002/2014JD022375.

784 Jiang, X., M. Zhao, and D. E. Waliser (2012), Modulation of tropical cyclone activity by the
785 tropical intraseasonal oscillation over the Eastern Pacific in a high resolution GCM, *J.*
786 *Climate*, *25*, 6524-6538.
787 Kiladis, G. N., J. Dias, K. H. Straub, M. C. Wheeler, S. N. Tulich, K. Kikuchi, K.M.
788 Weickmann, and M. J. Ventrice (2014), A comparison of OLR and circulation based
789 indices for tracking the MJO, *Mon. Wea. Rev.*, *142*, 1697-1715.
790 Khouider, B., and A. J. Majda (2006), A simple multicloud parameterization for convectively
791 coupled tropical waves. Part I: Linear analysis, *J. Atmos. Sci.*, *63*, 1308-1323.
792 Khouider, B., and A. J. Majda (2007), A simple multicloud parameterization for convectively
793 coupled tropical waves. Part II: Nonlinear simulations, *J. Atmos. Sci.*, *64*, 381-400.
794 Khouider, B., A. St-Cyr, A. J. Majda, and J. Tribbia (2011), The MJO and convectively coupled
795 waves in a course-resolution GCM with a simple multicloud parameterization, *J. Atmos.*
796 *Sci.*, *68*, 240-264.
797 Klingaman, N. P., and S. J. Woolnough (2014a), The role of air–sea coupling in the simulation
798 of the Madden–Julian oscillation in the Hadley Centre model, *Q. J. Roy. Meteor. Soc.*.
799 *140*, 2272–2286, doi:10.1002/qj.2295.
800 Klingaman, N. P., and S. J. Woolnough (2014b), Using a case-study approach to improve the
801 Madden–Julian oscillation in the Hadley Centre model, *Q. J. Roy. Meteor. Soc.*, *140*,
802 2491–2505, doi:10.1002/qj.2314.
803 Lau, K.-M., and P. H. Chan (1986), Aspects of the 40–50 day oscillation during the northern
804 summer as inferred from outgoing longwave radiation, *Mon. Wea. Rev.*, *114*, 1354-1367.
805 Lau, W. K. M., and D. E. Waliser (2005), Intraseasonal Variability in the Atmosphere-Ocean
806 Climate System, Springer, Heidelberg, Germany.

807 Madden, R. A., and P. R. Julian (1971), Detection of a 40-50 day oscillation in the zonal wind in
808 the tropical Pacific, *J. Atmos. Sci., 28*, 702-708.
809 Madden, R. A., and P. R. Julian (1972), Description of global-scale circulation cells in the
810 tropics with a 40–50 day period, *J. Atmos. Sci., 29*, 1109-1123.
811 Madden, R. A., and P. R. Julian (1994), Observations of the 40-50-day tropical oscillation – A
812 review, *Mon. Wea. Rev., 122*, 814-837.
813 Majda, A. J., and R. Klein (2003), Systematic multiscale models for the tropics, *J. Atmos. Sci.*,
814 *60*, 393-408.
815 Majda, A. J., and S. N. Stechmann (2009), The skeleton of tropical intraseasonal oscillations,
816 *Proc. Natl. Acad. Sci. USA, 106*, 8417-8422.
817 Majda, A. J., and S. N. Stechmann (2011), Nonlinear dynamics and regional variations in the
818 MJO skeleton, *J. Atmos. Sci.*, *68*, 3053-3071.
819 Maloney, E. D., and D. L. Hartmann (1998), Frictional moisture convergence in a composite life
820 cycle of the Madden–Julian oscillation, *J. Climate, 11*, 2387–2403.
821 Maloney, E. D., and D. L. Hartmann (2000), Modulation of eastern north Pacific hurricanes by
822 the Madden–Julian oscillation, *J. Climate, 13*, 1451-1460.
823 Matthews, A. J. (2000), Propagation mechanisms for the Madden-Julian oscillation, *Quart. J.*
824 *Roy. Meteor. Soc.*, *126*, 2637-2651.
825 Matthews, A. J. (2004), Intraseasonal variability over tropical Africa during northern summer, *J.*
826 *Climate*, *17*, 2427-2440.
827 Matthews, A. J. (2008) Primary and successive events in the Madden-Julian oscillation, *Quart. J.*
828 *Roy. Meteor. Soc.*, *134*, 439-453.

Matthews, A. J. and G. N. Kiladis (1999), The tropical–extratropical interaction between high-frequency transients and the Madden–Julian oscillation, *Mon. Wea. Rev.*, *127*, 661-677.

Myers, D. S., and D. E. Waliser (2003), Three-dimensional water vapor and cloud variations associated with the Madden–Julian oscillation during northern hemisphere winter, *J. Climate*, *16*, 929-950.

Ogrosky, H. R., and S. N. Stechmann (2015), The MJO skeleton model with observation-based background state and forcing, *Quart. J. Roy. Meteor. Soc.*, doi:10.1002/qj.2552, in press.

Pohl, B., and A. J. Matthews (2007), Observed changes in the lifetime and amplitude of the Madden–Julian oscillation associated with interannual ENSO sea surface temperature anomalies, *J. Climate*, *20*, 2659-2674.

Pritchard, M. S., and C. S. Bretherton (2014), Causal evidence that rotational moisture advection is critical to the superparameterized Madden–Julian oscillation, *J. Atmos. Sci.*, *71*, 800-815.

Ray, P., and C. Zhang (2010), A case study of the mechanics of extratropical influence on the initiation of the Madden–Julian oscillation, *J. Atmos. Sci.*, *67*, 515-528.

Reynolds, R.W., N. A. Rayner, T. M. Smith, D. C. Stokes, and W. Wang (2002), An improved in situ and satellite SST analysis for climate, *J. Climate*, *15*, 1609-1625.

Roundy, P. E., C. J. Schreck III, and M. A. Janiga (2009), Contributions of convectively coupled equatorial Rossby waves and Kelvin waves to the real-time multivariate MJO indices, *Mon. Wea. Rev.*, *470*, 469-478.

Slingo, J. M., et al. (1996), Intraseasonal oscillations in 15 atmospheric general circulation models: Results from an AMIP diagnostic subproject, *Climate Dynam.*, *12*, 325-357.

851 Stachnik, J. P., D. E. Waliser, and A. J. Majda (2015), Precursor environmental conditions
852 associated with the termination of Madden-Julian oscillation events, *J. Atmos. Sci.*, *72*,
853 1908-1931.
854 Stechmann, S. N., and A. J. Majda (2015), Identifying the skeleton of the Madden-Julian
855 oscillation in observational data, *Mon. Wea. Rev.*, *143*, 395–416.
856 Stechmann, S. N., and H. R. Ogrosky (2014), The Walker circulation, diabatic heating, and
857 outgoing longwave radiation, *Geophys. Res. Lett.*, *41*, 9097-9105,
858 doi:10.1002/2014GL062257.
859 Straub, K. H. (2013), MJO initiation in the real-time multivariate MJO index, *J. Climate, 26*,
860 1130-1151.
861 Thual, S., and A. J. Majda (2015), A skeleton model for the MJO with refined vertical structure,
862 *Climate Dynam.*, doi: 10.1007/s00382-015-2731-x, in press.
863 Thual, S., A. J. Majda, and S. N. Stechmann (2014), A stochastic skeleton model for the MJO, *J.*
864 *Atmos. Sci.*, *71*, 697-715.
865 Thual, S., A. J. Majda, and S. N. Stechmann (2015), Asymmetric intraseasonal events in the
866 stochastic skeleton MJO model with seasonal cycle, *Climate Dynam.*, *45*, 603-618, doi:
867 10.1007/s00382-014-2256-8.
868 Ventrice, M. J., M. C. Wheeler, H. H. Hendon, C. J. Schreck III, C. D. Thorncroft, and G. N.
869 Kiladis (2013), A modified multivariate Madden–Julian oscillation index using velocity
870 potential, *Mon. Wea. Rev.*, *141*, 4197–4210.
871 Waliser, D. E., C. Jones, J.-K. E. Schemm, and N. E. Graham (1999), A statistical extended-
872 range tropical forecast model based on the slow evolution of the Madden–Julian
873 oscillation, *J. Climate*, *12*, 1918-1939.

874 Waliser, D., et al. (2009), MJO simulation diagnostics, *J. Climate*, *22*, 3006–3030
875 Wang, L., K. Kodera, and W. Chen (2012), Observed triggering of tropical convection by a cold
876 surge: Implications for MJO initiation, *Q. J. Roy. Meteorol. Soc.*, *138*, 1740-1750.
877 Wheeler, M. C., and H. H. Hendon (2004), An all-season real-time multivariate MJO index:
878 Development of an index for monitoring and prediction, *Mon. Wea. Rev.*, *132*, 1917-
879 1932.
880 Wheeler, M. C., G. N. Kiladis, and P. J. Webster (2000), Large-scale dynamical fields associated
881 with convectively coupled equatorial waves, *J. Atmos. Sci.*, *57*, 613-640.
882 Yoneyama, K., C. Zhang, and C. N. Long (2013), Tracking pulses of the Madden–Julian
883 oscillation, *Bull. Amer. Meteor. Soc.*, *94*, 1871–-891.
884 Zhang, C. (2005), Madden-Julian oscillation, *Rev. Geophys.*, *43*, RG2003,
885 doi:10.1029/2004RG000158.
886 Zhang, C., M. Dong, S. Gualdi, H. H. Hendon, E. D. Maloney, A. Marshall, K. R. Sperber, and
887 W. Wang (2006), Simulations of the Madden-Julian oscillation in four pairs of coupled
888 and uncoupled models, *Climate Dynam.*, *27*, 573-592.

889 **Figure Captions**

890 **Figure 1**. The shape of (a) the idealized warm pool (i.e., Case-WP) and (b) annual average
891 (1971-2000) NOAA OI SSTs v2 used to force the skeleton model. The observed SSTs have been
892 meridionally averaged from 10°S-10°N with a Poisson relaxation and interpolated over missing
893 data (i.e., land). The solid line in (b) indicates the average SSTs from all waves downscaled to
894 the model resolution of 625 km. The dashed profile in (b) has been smoothed to only retain the
895 first eight Fourier modes (Case-SST8N).

896

897 **Figure 2**. (a)-(c) Hovmöller diagrams of the anomalous 20-100 day filtered skeleton model
898 variables for a 600 day period taken from the idealized warm pool simulation (Case-WP). All
899 variables have daily resolution and are shown in dimensional units for the reconstructed (a)
900 convective heating ($\bar{H}a$), (b) zonal wind (u), and (c) moisture (q) variables. (d)-(f) As in (a)-(c),
901 but for the model simulation using the truncated, observed SSTs (Case-SST8N).

902

903 **Figure 3**. Zonal wavenumber-frequency power spectra of the (a) convective heating ($\bar{H}a$, K day^{-1})
904 and (b) zonal wind (u, m s^{-1}) for the idealized warm pool case (Case-WP) from the skeleton
905 model. Shading indicates the base-10 logarithm for the reconstructed and dimensional variables
906 taken at the equator for approximately 34 years of model data. The black circles mark the
907 dispersion curves from a separate stability analysis of the linear waves in the skeleton model in
908 the Indian Ocean (67.5°E). The dashed, black lines indicate periods of 30 and 90 days. (c)-(d) As
909 in (a)-(b), but for the model simulation using the truncated, observed SSTs (Case-SST8N).

910

Figure 4. (a)-(b) The first two leading modes from a univariate EOF analysis of the 20-100 day filtered convective heating ($\overline{H}a$) anomalies along the equator from approximately 340 years of the idealized warm pool simulation (Case-WP). (c)-(d) As in (a)-(b), but for a univariate EOF analysis of the zonal wind (u). The percent variance explained by each mode is shown in the upper-right of each panel.

Figure 5. (a)-(b) The first two leading modes from a multivariate EOF analysis of the 20-100 day filtered convective heating ($-\overline{H}a$) and zonal wind (u) model anomalies along the equator from approximately 340 years of the idealized warm pool simulation (Case-WP). The order of EOF1 and EOF2 have been interchanged in addition to switching the sign of the convective heating term to better match the *Wheeler and Hendon* [2004] EOFs. (c)-(d) The first leading two modes from the observed multivariate analysis of *Wheeler and Hendon* [2004] showing the 15°S-15°N EOF structures of OLR and zonal wind at 850 hPa and 200 hPa (u850 and u200, respectively). The percent variance explained by each mode is shown in the upper-right of each panel.

Figure 6. (a)-(b) As in Figure 5, but for the model simulation using the truncated, observed SSTs (Case-SST8N). Panels (c)-(d) are identical to Figure 5 to better facilitate comparison between the modeled and observed EOFs.

Figure 7. Lag correlations between the corresponding PC1 and PC2 from the multivariate EOF analysis of approximately 340 years of the model simulation using the truncated, observed SSTs (Case-SST8N).

Figure 8. Examples of two MJO events using the skeleton multivariate MJO (SMM) index and the event criteria defined in *Stachnik et al.* [2015] for the model simulation using an idealized warm pool (Case-WP). The daily values of SMM1 and SMM2 (i.e., the principal components) are plotted as small dots for (a) day 30561-30619 and (b) day 32662-32734 in the 2-dimensional phase space obtained when projecting the model data onto the observed EOF patterns of *Wheeler and Hendon* [2004]. The initiation of a primary MJO event is shown in gray and indicated with a large, circumscribed X while the corresponding termination event is shown in red for each panel. Continuing MJO events are shown in blue, green, and orange in (a), with the subsequent history of the SMM index highlighted through the following four phases. The beginning of each continuing event are shown with large, blue markers in (b) along with the start of a circumnavigating event and associated path highlighted in gold.

Figure 9. Cumulative probability distribution functions of the observed and modeled MJO event lengths from the stochastic model simulation using the truncated, observed SSTs (Case-SST8N), and a deterministic model simulation using the same SSTs (Case-SST8Ndet). The observed distribution is based on the historical *Wheeler and Hendon* [2004] RMM index from 1979-2012 and is represented by a thick, black line. The corresponding model event length distributions for similar 34 year periods are shown using thin, blue and red lines for the stochastic and deterministic solutions, respectively.

Figure 10. Radial-frequency plots showing the percent occurrence of MJO events as a function of RMM phase for (a) observations (1979-2012) and single 34 year periods from the stochastic model simulations using (b) an idealized warm pool (Case-WP) and (c) truncated, observed SSTs

(Case-SST8N). (d) As in (c), but for the deterministic model simulation using the truncated, observed SSTs (Case-SST8Ndet). The black dots plotted at the center angle of each phase indicate the frequency of occurrence and are connected only for the ease of viewing primary, continuing, and terminal MJO events (gray, blue, and red lines, respectively). Range rings represent the 1%, 5%, 10%, 15%, and 20% frequencies of occurrence from the center to edge of the diagram, respectively.

Figure 11. The mean frequency and uncertainty estimates of primary (gray), continuing (blue), and terminal (red) MJO events for each RMM phase in (a) observations and (b)-(f) approximately 680 years of model data. Simulations using an idealized warm pool and the truncated, observed SSTs (Case-WP and Case-SST8N, respectively) are shown in panels (b)-(c) with a special simulation using a homogeneous background state (Case-HG) in (d). Results from a deterministic version of the skeleton model using the idealized warm pool (Case-WPdet) and truncated, observed SSTs (Case-SST8Ndet) are shown in (e)-(f). The dashed line indicates the 12.5% frequency and represents the equal likelihood of an MJO event occurring in any phase. Error bars indicate the 95% uncertainty estimates and are calculated from a binomial proportion confidence interval (see text for details). The total number of primary/terminal and continuing events are indicated in the top right of each panel.

Figure 12. Initiation composites of the RMM1-RMM2 paths for (a) observations (1979-2012) and SMM1-SMM2 for an equivalent 34 year period from the stochastic model simulations using (b) an idealized warm pool (Case-WP) and (c) the truncated, observed SSTs (Case-SST8N). (d) As in (c), but for the deterministic model simulation using the truncated and observed SSTs

(Case-SST8Ndet). The composite values for a primary event are marked with a circumscribed X for each phase. The composite history before (3 days) and after (12 days) the initiation event (i.e., first day after the combined amplitude grows above unity) are shown in different colors for each phase. The composite daily RMM and SMM values are plotted using small dots, while closed squares appear every three days for reference.

Figure 13. As in Figure 12, but for MJO termination events. The composite values for a termination event are marked with a circumscribed X for each phase. The composite history before (12 days) and after (3 days) the termination event (i.e., last day before the combined amplitude decays below unity) are shown in different colors for each phase.

Figure 14. Longitude-lag composites of the 20-100 day filtered anomalous (a)-(b) convective heating ($\overline{H}a$), (d)-(e) moisture variable (q), and (g)-(h) zonal wind (u) from the model simulation using the truncated, observed SSTs (Case-SST8N) for RMM phase 6 continuing and terminal MJO events. All data are taken along the equator and composited for approximately 340 years. Differences between terminal and continuing MJO events are shown in panels (c), (f), and (i) for $\overline{H}a$, q, and u, respectively. The stippling in the difference panels indicates the presence of a statistically significant different local mean for the continuing and terminating events (see *Stachnik et al.* [2015] for further details). The number of events used for each composite (N) is listed in the top-right corner of each panel.

Figure 15. As in Figure 14, but for the (a)-(c) zonal convergence and (d)-(f) potential temperature (θ). (g)-(i) As in (d)-(f), but for a shorter, single 34 year period of skeleton model data.

Figure 16. Box-whisker diagrams showing the distribution of (a) zonal wind (u) and (b) moisture variable (q) anomalies for RMM phase 6 continuing and terminating MJO events averaged over the local domain (120-160°E) at day -10. Box lines indicate the 25%, 50%, and 75% percentiles with whiskers indicating the minimum and maximum values for all events. The blue circles and red triangles represent the local-domain average values for individual continuing and terminating MJO events, respectively. The mean quantities for each event type are overlaid with a black star. All data are taken along the equator and represent 34 years of simulated MJO events using the truncated, observed SSTs (Case-SST8N).

Table 1. Maximum correlation coefficient for the longitudinal structure of the leading two EOFs from all lags between the skeleton model and observed *Wheeler and Hendon* [2004] RMM index

	EOF Variable		
EOF	Univariate (u)	Multivariate (u)	Multivariate ($-\bar{H}a$)
		Case-WP	
EOF1	0.85	0.83	0.70
EOF2	0.74	0.72	0.68
		Case-SST8N	
EOF1	0.98	0.98	0.89
EOF2	0.93	0.94	0.80

1017 **Table 2**. Number of MJO events and average event length from observations (1979-2012) [a] and

1018 an equivalent 34 year period[b] from the stochastic skeleton model for the simulation using an

1019 idealized warm pool (Case-WP) as a function of EOFs used to calculate the SMM index

	Event type (#)				
EOFs	Primary	Continuing	Circum-navigating	Terminal	Event length (d)
Univariate (*u*)	89.3±4.3	309.2±23.4	21.2±3.1	89.3±4.3	39.5±1.6
Multivariate (Model)	91.4±3.9	341±22.9	23.5±3.0	91.4±3.9	39.9±1.4
Multivariate (WH04[c])	97.7±3.5	343.4±17.9	23.7±2.0	97.7±3.5	40.2±1.1
Observations	154	330	15	154	34.9

1020

1021 [a]The observed MJO event numbers are taken from *Stachnik et al.* [2015]

1022 [b]The model statistics and uncertainty estimates are generated from 680 years of model data

1023 comprising 20 independent samples of 34 year periods

1024 [c]WH04 refers to the case in which the observed *Wheeler and Hendon* [2004] EOFs are used in

1025 place of the model quantities to calculate the SMM index

1026 **Table 3**. As in Table 2, but for the simulation using the truncated, observed SSTs (Case-SST8N)

	Event type (#)				
EOFs	Primary	Continuing	Circum-navigating	Terminal	Event length (d)
Univariate (*u*)	98.3±2.8	443.5±31.5	33.4±3.6	98.3±2.8	43.3±1.7
Multivariate (Model)	98.4±3.2	466.8±31.2	35.5±3.4	98.4±3.2	43.8±1.5
Multivariate (WH04)	97.7±3.6	477.9±33.2	36.6±3.5	97.7±3.6	44.2±1.6
Observations	154	330	15	154	34.9

1027

Table 4. Number of MJO events and average event length from observations (1979-2012) and an equivalent 34 year period from the stochastic and deterministic skeleton model simulations using the idealized warm pool (Case-WP and Case-WPdet) and truncated, observed SSTs (Case-SST8N and Case-SST8Ndet) projected on the observed *Wheeler and Hendon* [2004] RMM EOFs

	Event type (#)				
Dataset	Primary	Continuing	Circum-navigating	Terminal	Event length (d)
Case-WP	97.7±3.5	343.4±17.9	23.7±2.0	97.7±3.5	40.2±1.1
Case-SST8N	97.7±3.6	477.9±33.2	36.6±3.5	97.7±3.6	44.2±1.6
Case-WPdet	90.8±2.3	797.3±29.0	75.3±3.7	90.8±2.3	61.5±2.2
Case-SST8Ndet	87.4±1.9	1316.7±26.6	140.1±3.2	87.4±1.9	77.7±1.8
Observations	154	330	15	154	34.9

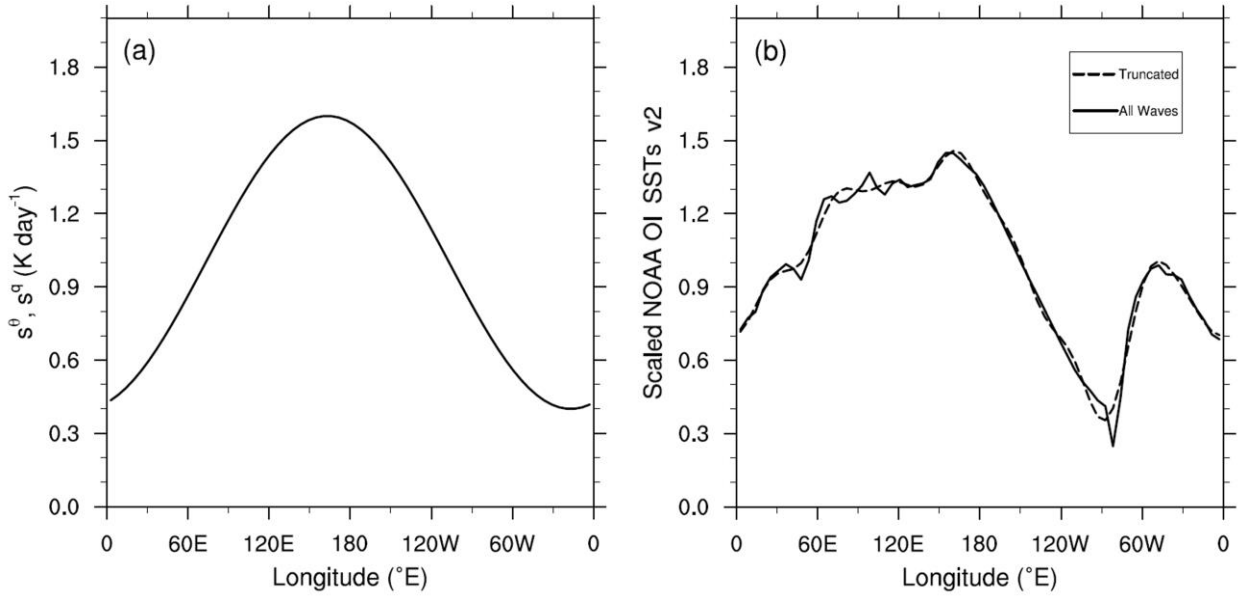

Figure 1. The shape of (a) the idealized warm pool (i.e., Case-WP) and (b) annual average (1971-2000) NOAA OI SSTs v2 used to force the skeleton model. The observed SSTs have been meridionally averaged from 10°S-10°N with a Poisson relaxation and interpolated over missing data (i.e., land). The solid line in (b) indicates the average SSTs from all waves downscaled to the model resolution of 625 km. The dashed profile in (b) has been smoothed to only retain the first eight Fourier modes (Case-SST8N).

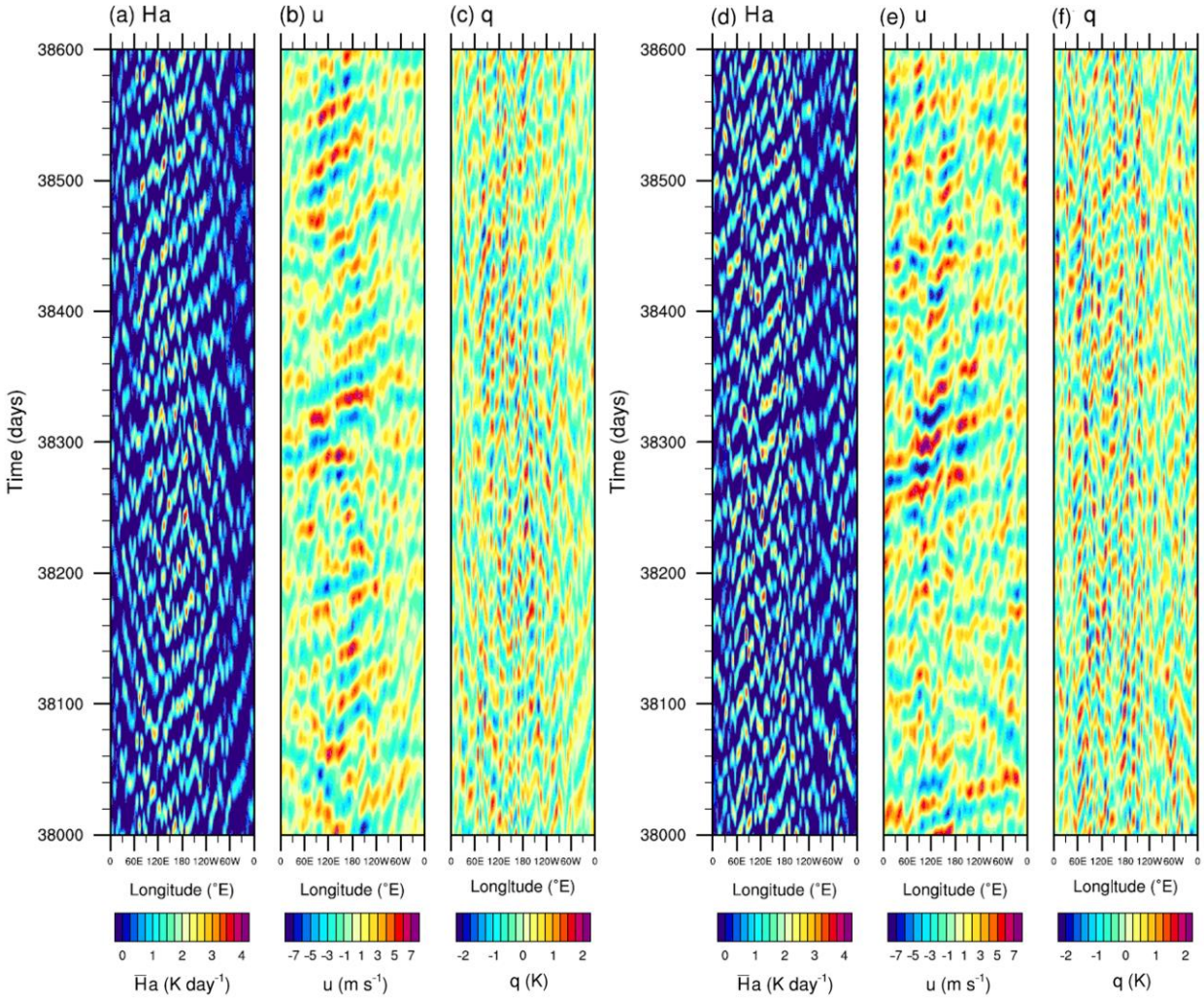

Figure 2. (a)-(c) Hovmöller diagrams of the anomalous 20-100 day filtered skeleton model variables for a 600 day period taken from the idealized warm pool simulation (Case-WP). All variables have daily resolution and are shown in dimensional units for the reconstructed (a) convective heating ($\overline{Ha}$), (b) zonal wind (u), and (c) moisture (q) variables. (d)-(f) As in (a)-(c), but for the model simulation using the truncated, observed SSTs (Case-SST8N).

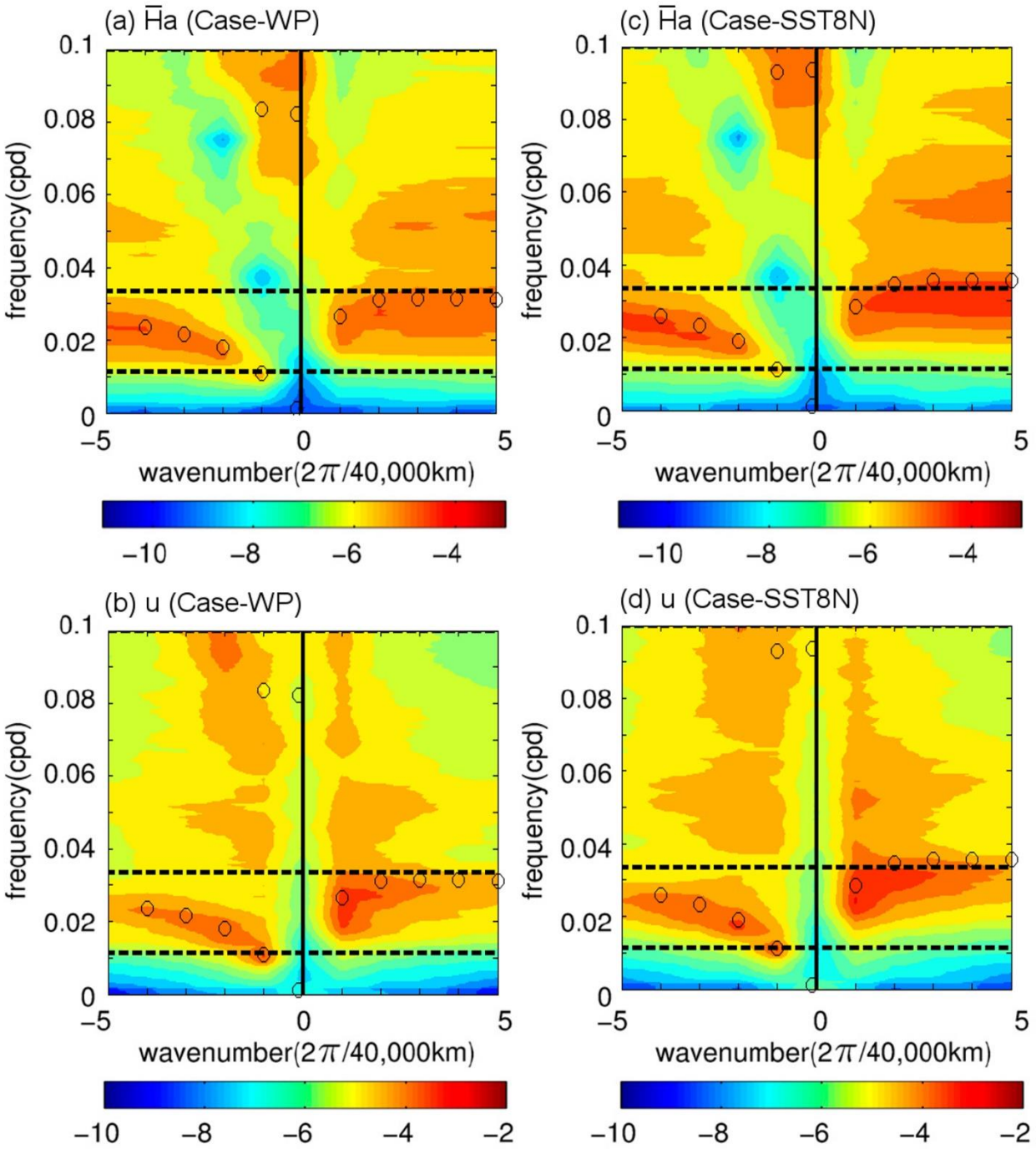

Figure 3. Zonal wavenumber-frequency power spectra of the (a) convective heating ($\bar{H}a$, K day^{-1}) and (b) zonal wind (u, m s^{-1}) for the idealized warm pool case (Case-WP) from the skeleton model. Shading indicates the base-10 logarithm for the reconstructed and dimensional variables taken at the equator for approximately 34 years of model data. The black circles mark the dispersion curves from a separate stability analysis of the linear waves in the skeleton model in the Indian Ocean (67.5°E). The dashed, black lines indicate periods of 30 and 90 days. (c)-(d) As in (a)-(b), but for the model simulation using the truncated, observed SSTs (Case-SST8N).

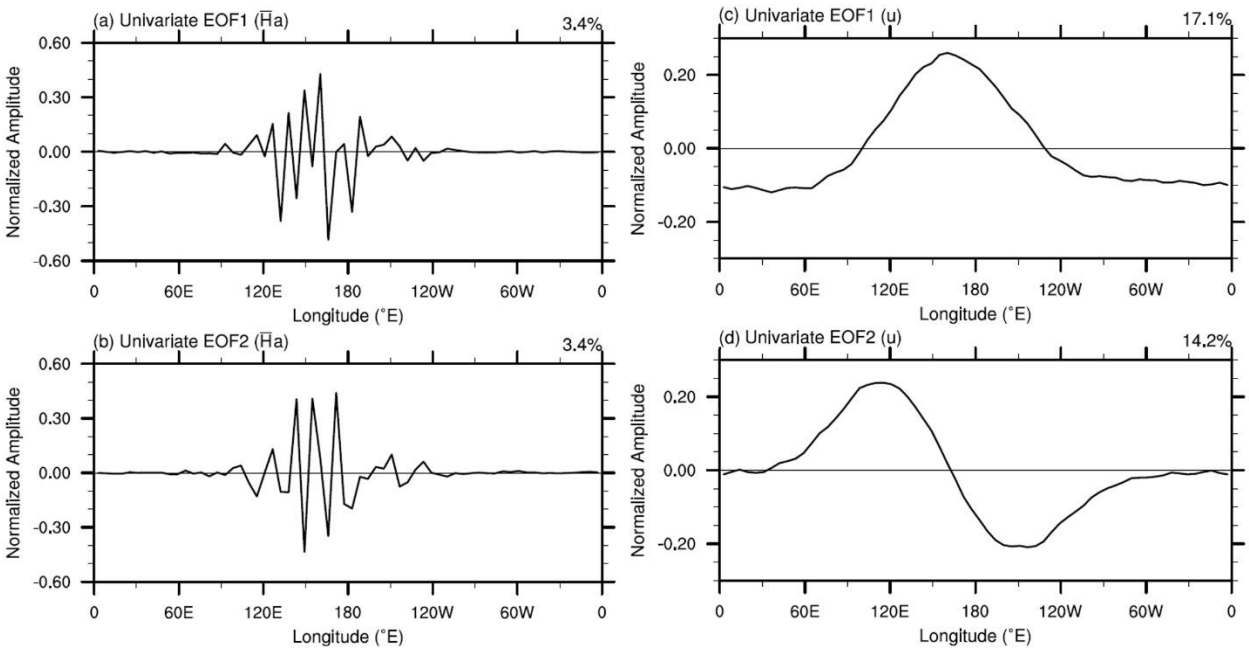

Figure 4. (a)-(b) The first two leading modes from a univariate EOF analysis of the 20-100 day filtered convective heating ($\overline{Ha}$) anomalies along the equator from approximately 340 years of the idealized warm pool simulation (Case-WP). (c)-(d) As in (a)-(b), but for a univariate EOF analysis of the zonal wind (u). The percent variance explained by each mode is shown in the upper-right of each panel.

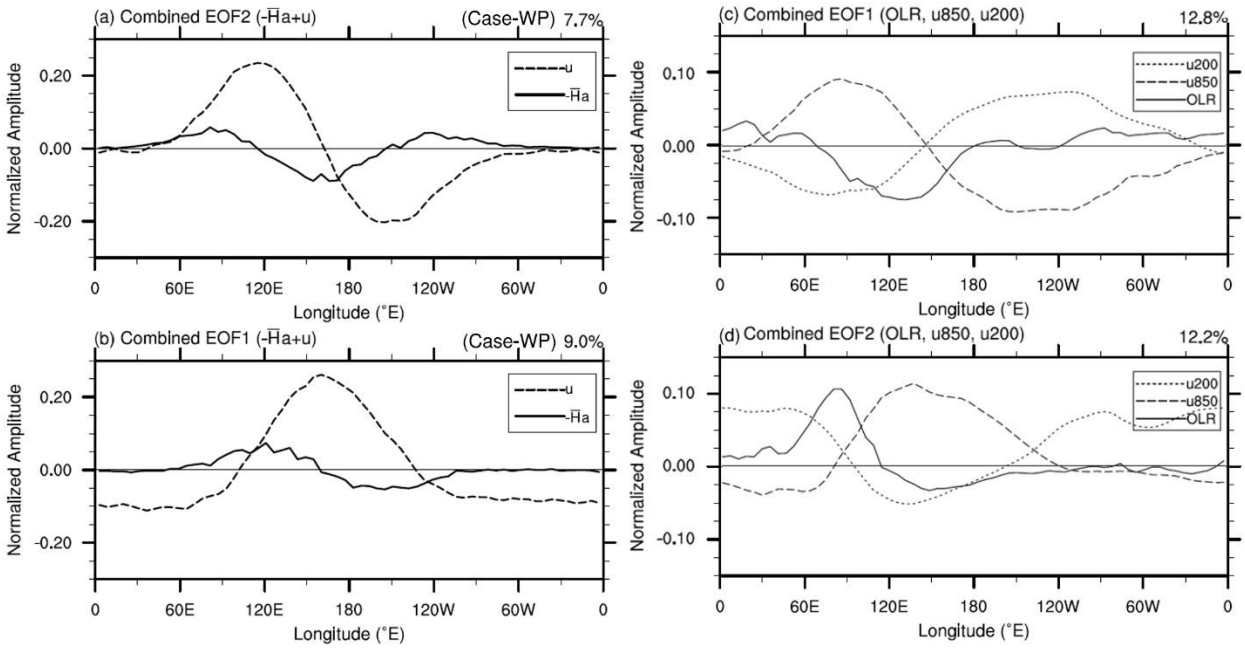

Figure 5. (a)-(b) The first two leading modes from a multivariate EOF analysis of the 20-100 day filtered convective heating ($-\overline{H}a$) and zonal wind (u) model anomalies along the equator from approximately 340 years of the idealized warm pool simulation (Case-WP). The order of EOF1 and EOF2 have been interchanged in addition to switching the sign of the convective heating term to better match the *Wheeler and Hendon* [2004] EOFs. (c)-(d) The first leading two modes from the observed multivariate analysis of *Wheeler and Hendon* [2004] showing the 15°S-15°N EOF structures of OLR and zonal wind at 850 hPa and 200 hPa (u850 and u200, respectively). The percent variance explained by each mode is shown in the upper-right of each panel.

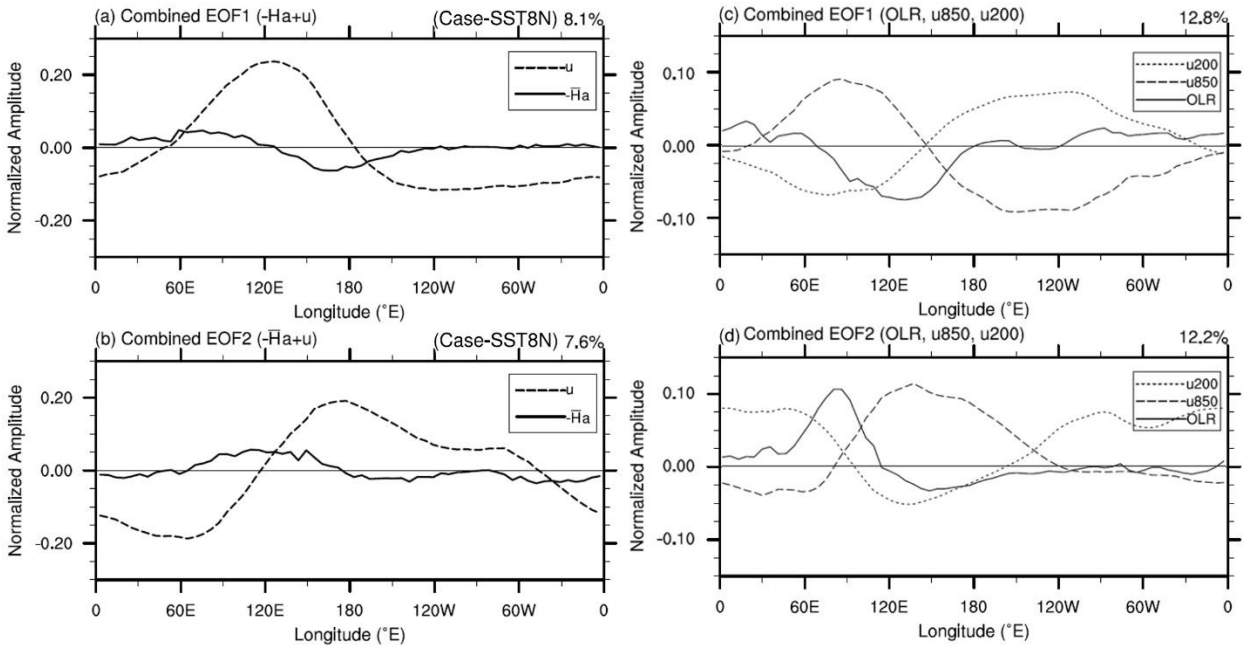

Figure 6. (a)-(b) As in Figure 5, but for the model simulation using the truncated, observed SSTs (Case-SST8N). Panels (c)-(d) are identical to Figure 5 to better facilitate comparison between the modeled and observed EOFs.

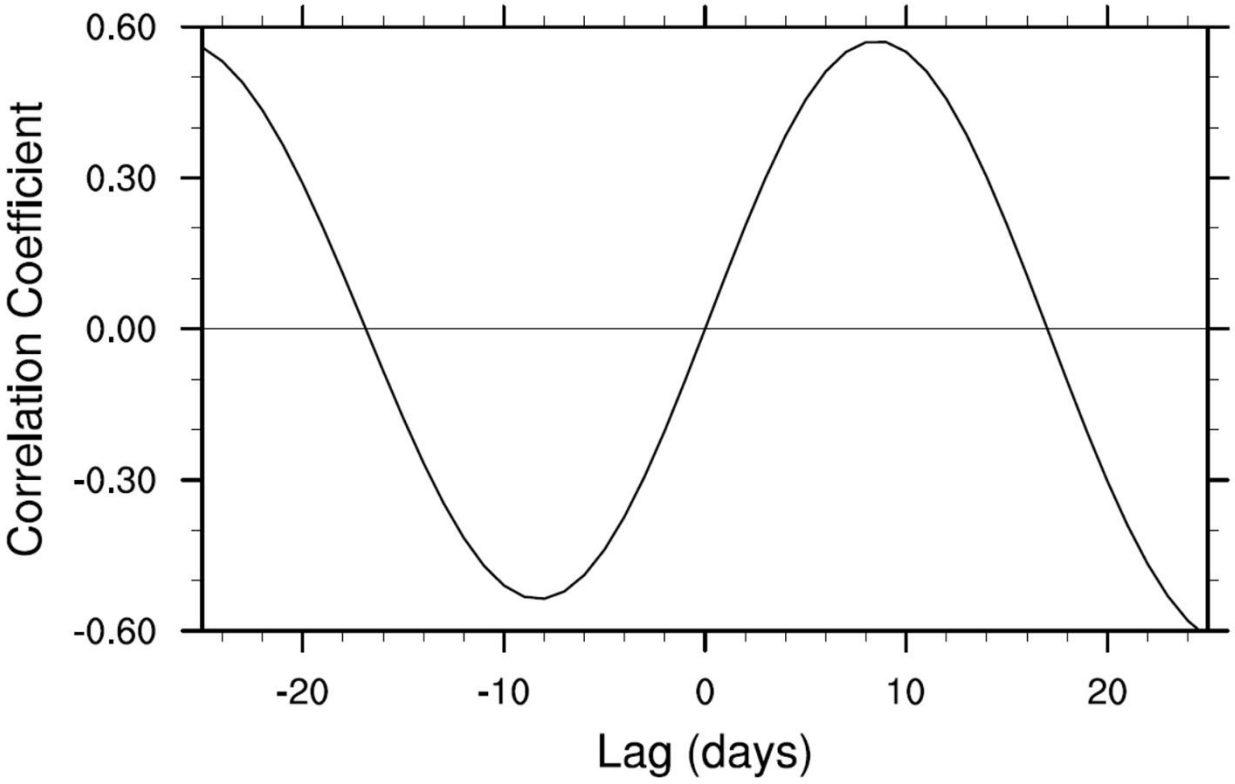

Figure 7. Lag correlations between the corresponding PC1 and PC2 from the multivariate EOF analysis of approximately 340 years of the model simulation using the truncated, observed SSTs (Case-SST8N).

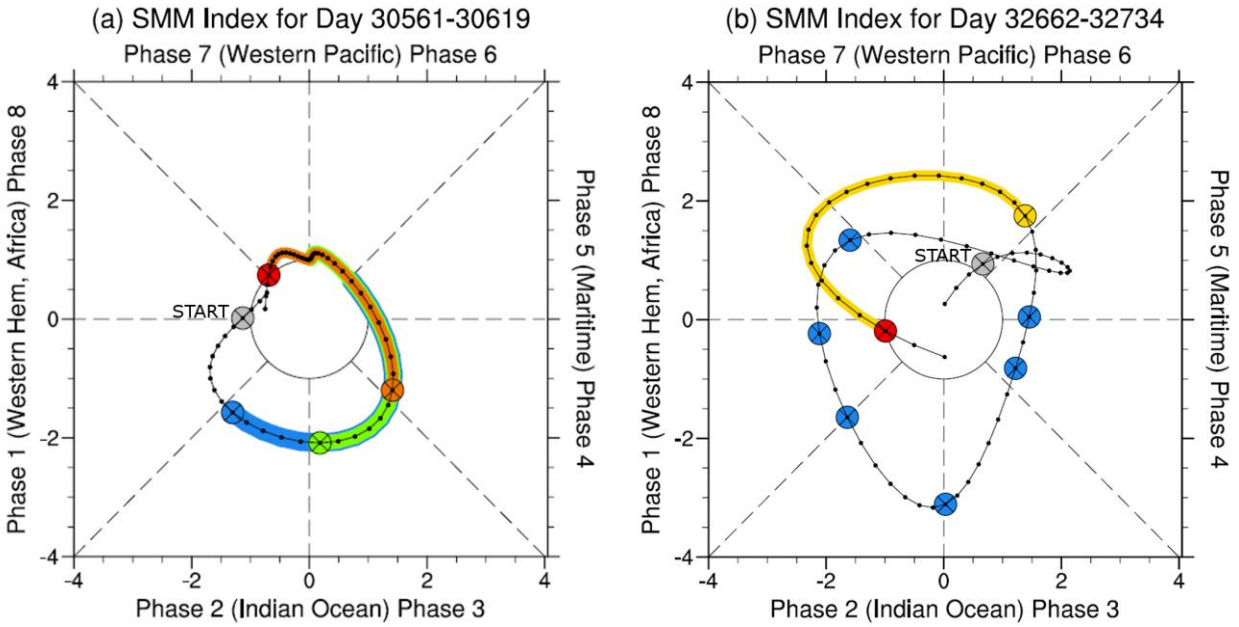

Figure 8. Examples of two MJO events using the skeleton multivariate MJO (SMM) index and the event criteria defined in *Stachnik et al.* [2015] for the model simulation using an idealized warm pool (Case-WP). The daily values of SMM1 and SMM2 (i.e., the principal components) are plotted as small dots for (a) day 30561-30619 and (b) day 32662-32734 in the 2-dimensional phase space obtained when projecting the model data onto the observed EOF patterns of *Wheeler and Hendon* [2004]. The initiation of a primary MJO event is shown in gray and indicated with a large, circumscribed X while the corresponding termination event is shown in red for each panel. Continuing MJO events are shown in blue, green, and orange in (a), with the subsequent history of the SMM index highlighted through the following four phases. The beginning of each continuing event are shown with large, blue markers in (b) along with the start of a circumnavigating event and associated path highlighted in gold.

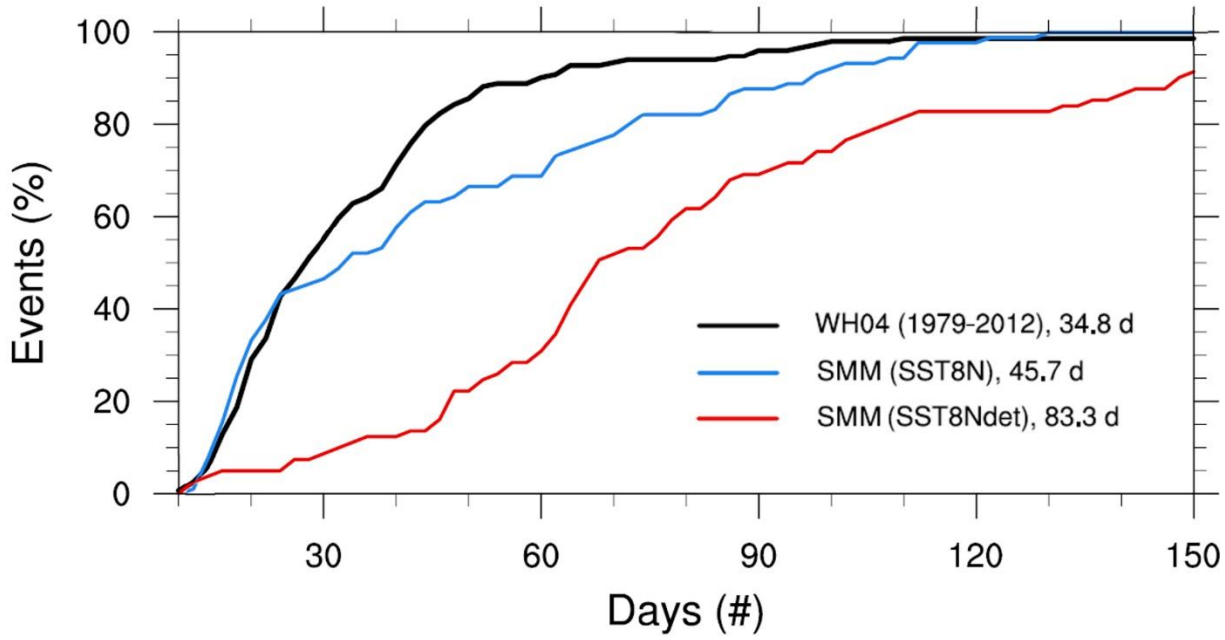

Figure 9. Cumulative probability distribution functions of the observed and modeled MJO event lengths from the stochastic model simulation using the truncated, observed SSTs (Case-SST8N), and a deterministic model simulation using the same SSTs (Case-SST8Ndet). The observed distribution is based on the historical *Wheeler and Hendon* [2004] RMM index from 1979-2012 and is represented by a thick, black line. The corresponding model event length distributions for similar 34 year periods are shown using thin, blue and red lines for the stochastic and deterministic solutions, respectively.

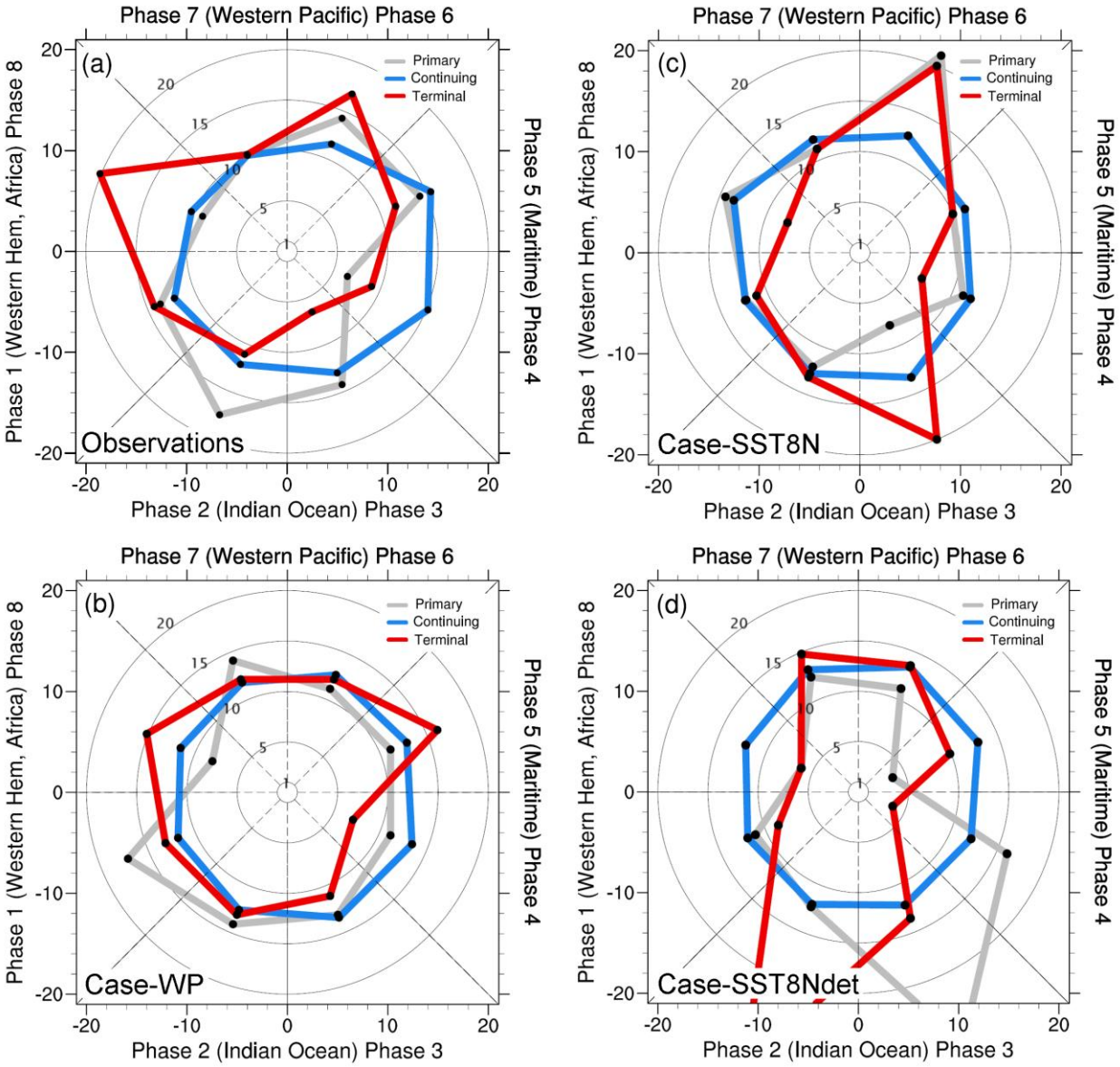

Figure 10. Radial-frequency plots showing the percent occurrence of MJO events as a function of RMM phase for (a) observations (1979-2012) and single 34 year periods from the stochastic model simulations using (b) an idealized warm pool (Case-WP) and (c) truncated, observed SSTs (Case-SST8N). (d) As in (c), but for the deterministic model simulation using the truncated, observed SSTs (Case-SST8Ndet). The black dots plotted at the center angle of each phase indicate the frequency of occurrence and are connected only for the ease of viewing primary, continuing, and terminal MJO events (gray, blue, and red lines, respectively). Range rings represent the 1%, 5%, 10%, 15%, and 20% frequencies of occurrence from the center to edge of the diagram, respectively.

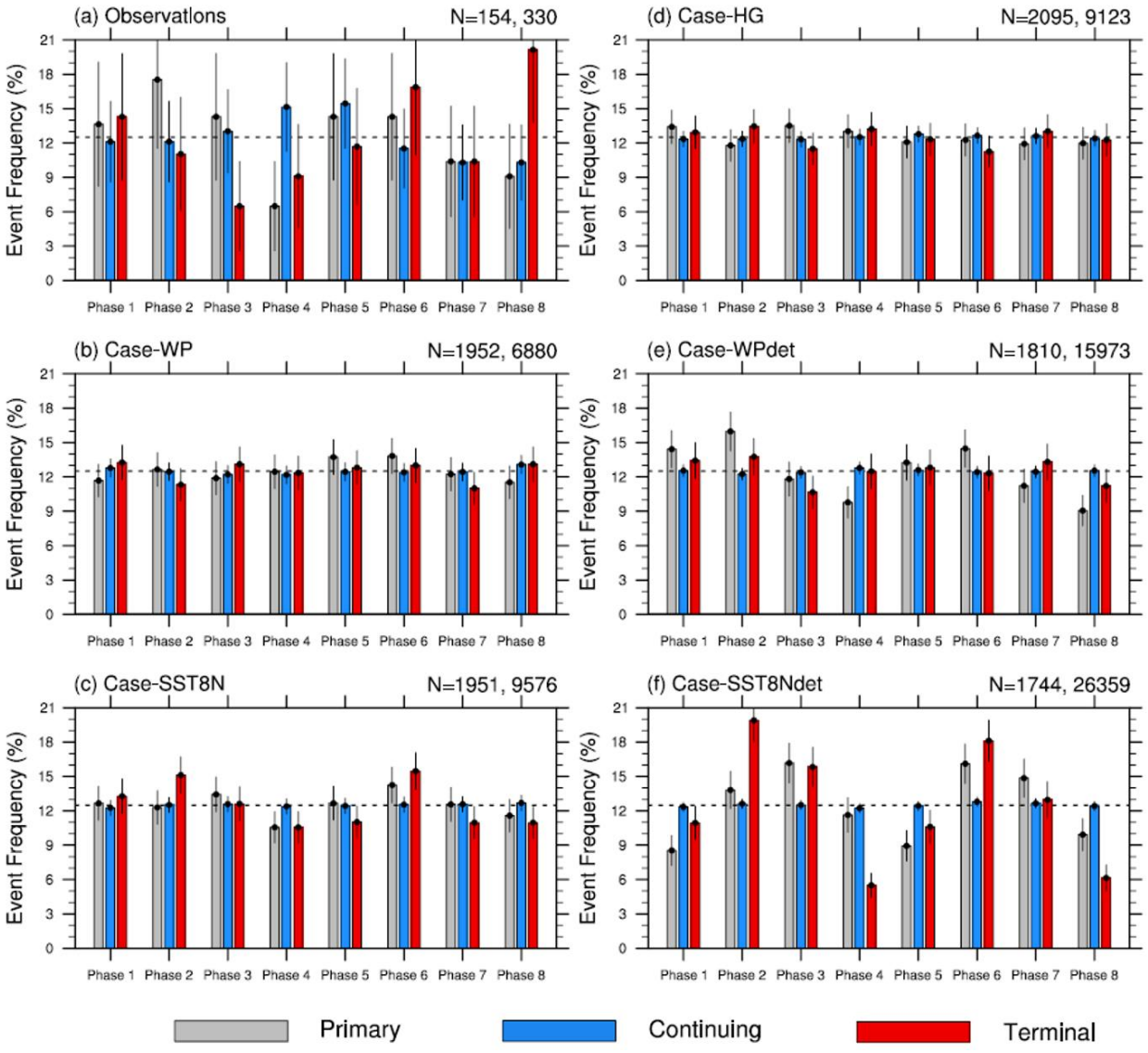

Figure 11. The mean frequency and uncertainty estimates of primary (gray), continuing (blue), and terminal (red) MJO events for each RMM phase in (a) observations and (b)-(f) approximately 680 years of model data. Simulations using an idealized warm pool and the truncated, observed SSTs (Case-WP and Case-SST8N, respectively) are shown in panels (b)-(c) with a special simulation using a homogeneous background state (Case-HG) in (d). Results from a deterministic version of the skeleton model using the idealized warm pool (Case-WPdet) and truncated, observed SSTs (Case-SST8Ndet) are shown in (e)-(f). The dashed line indicates the 12.5% frequency and represents the equal likelihood of an MJO event occurring in any phase. Error bars indicate the 95% uncertainty estimates and are calculated from a binomial proportion confidence interval (see text for details). The total number of primary/terminal and continuing events are indicated in the top right of each panel.

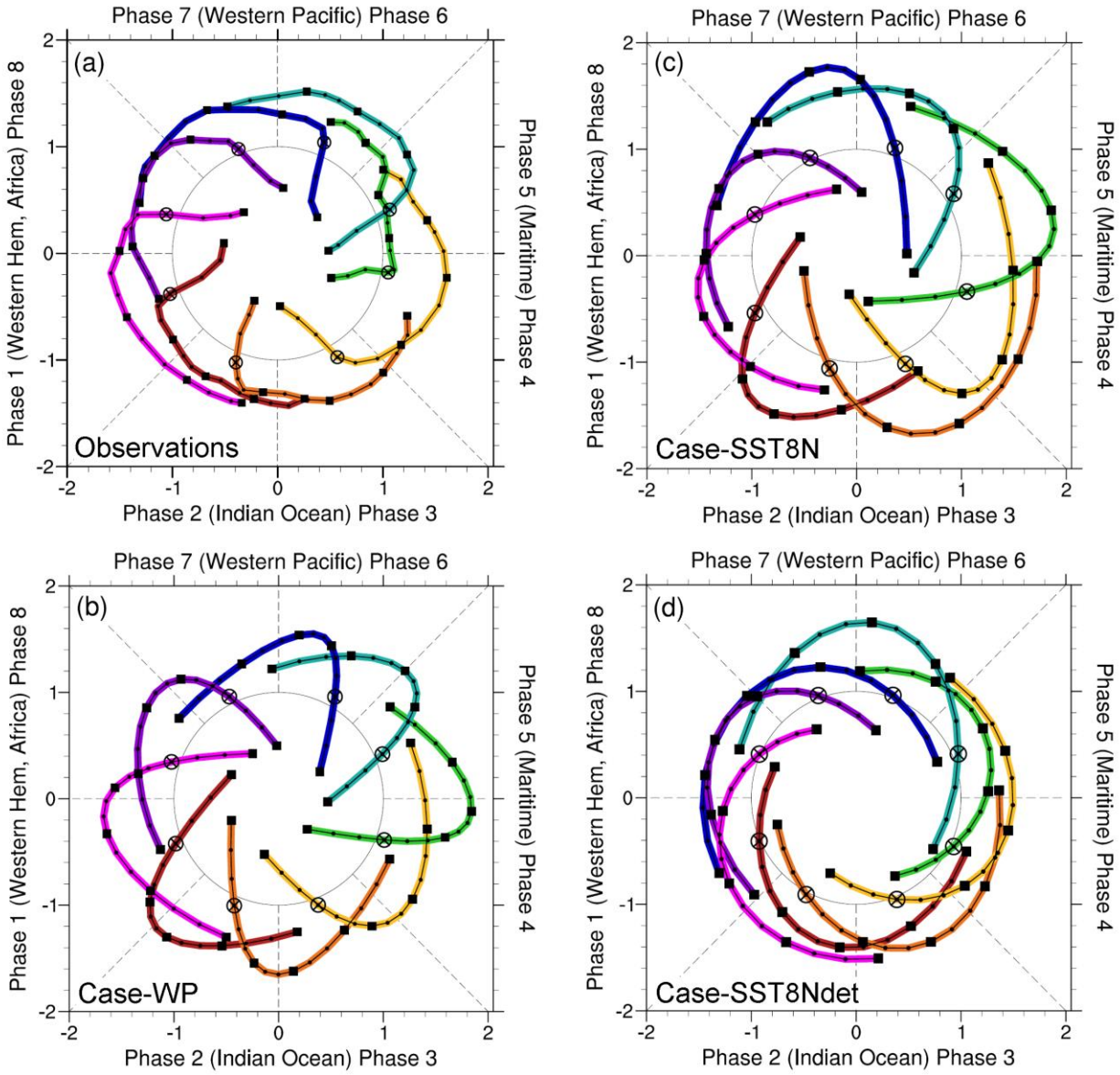

Figure 12. Initiation composites of the RMM1-RMM2 paths for (a) observations (1979-2012) and SMM1-SMM2 for an equivalent 34 year period from the stochastic model simulations using (b) an idealized warm pool (Case-WP) and (c) the truncated, observed SSTs (Case-SST8N). (d) As in (c), but for the deterministic model simulation using the truncated and observed SSTs (Case-SST8Ndet). The composite values for a primary event are marked with a circumscribed X for each phase. The composite history before (3 days) and after (12 days) the initiation event (i.e., first day after the combined amplitude grows above unity) are shown in different colors for each phase. The composite daily RMM and SMM values are plotted using small dots, while closed squares appear every three days for reference.

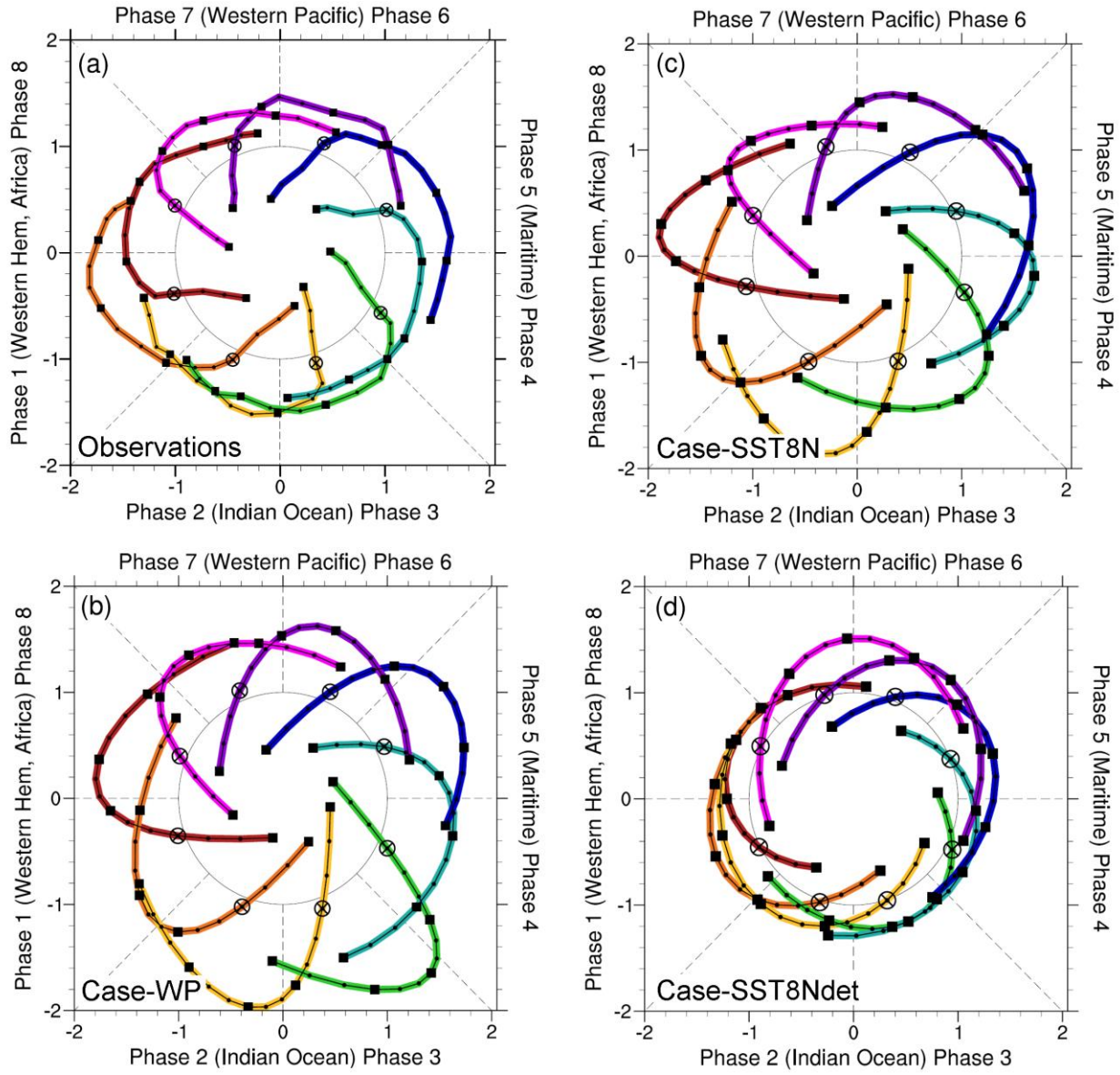

Figure 13. As in Figure 12, but for MJO termination events. The composite values for a termination event are marked with a circumscribed X for each phase. The composite history before (12 days) and after (3 days) the termination event (i.e., last day before the combined amplitude decays below unity) are shown in different colors for each phase.

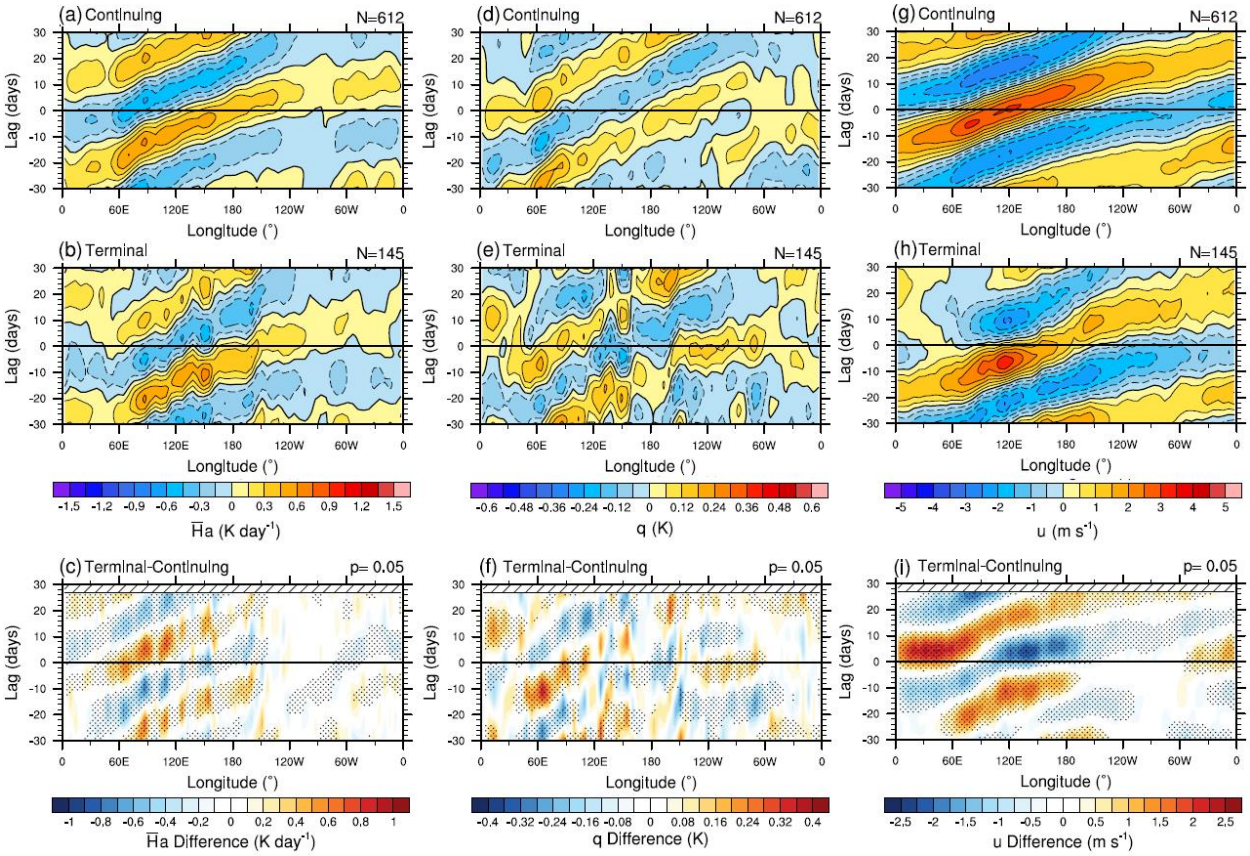

Figure 14. Longitude-lag composites of the 20-100 day filtered anomalous (a)-(b) convective heating ($\bar{H}a$), (d)-(e) moisture variable (q), and (g)-(h) zonal wind (u) from the model simulation using the truncated, observed SSTs (Case-SST8N) for RMM phase 6 continuing and terminal MJO events. All data are taken along the equator and composited for approximately 340 years. Differences between terminal and continuing MJO events are shown in panels (c), (f), and (i) for $\bar{H}a$, q, and u, respectively. The stippling in the difference panels indicates the presence of a statistically significant different local mean for the continuing and terminating events (see *Stachnik et al.* [2015] for further details). The number of events used for each composite (N) is listed in the top-right corner of each panel.

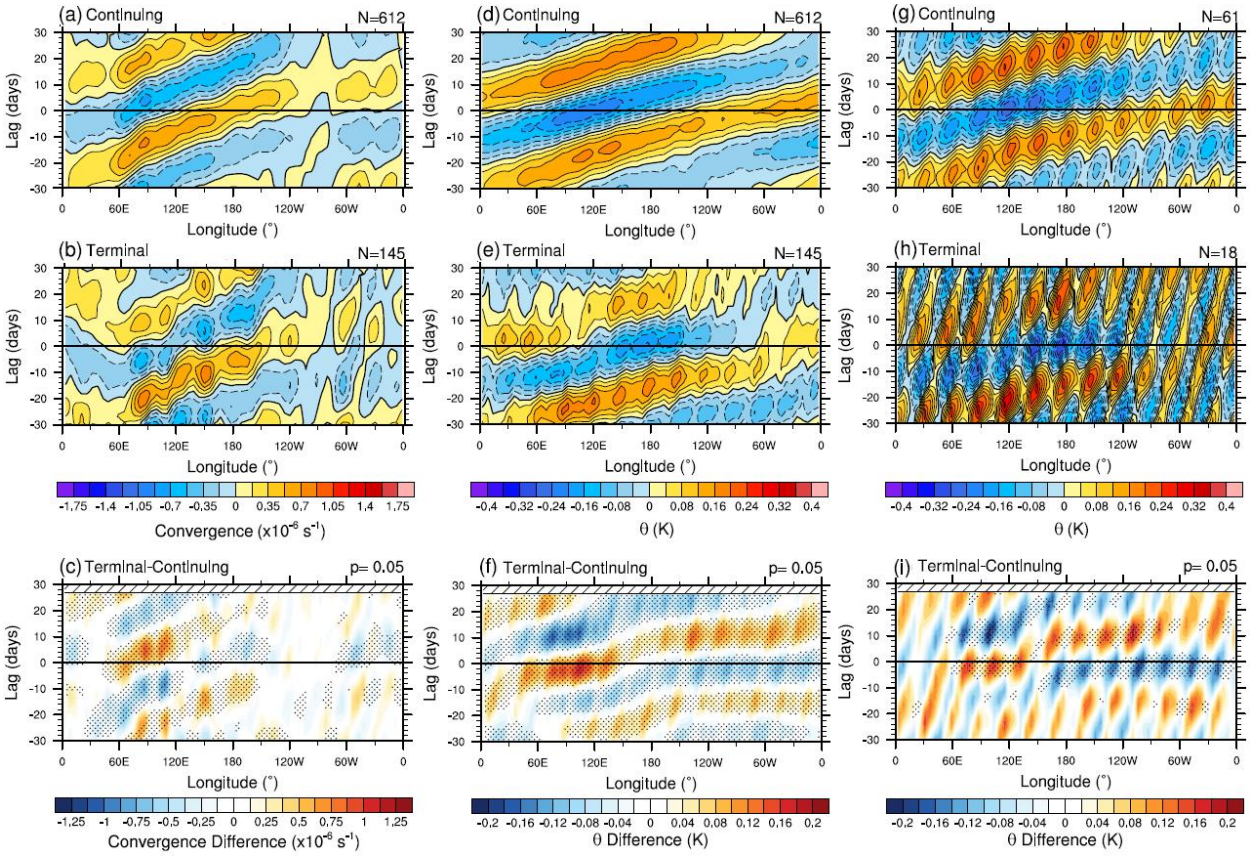

Figure 15. As in Figure 14, but for the (a)-(c) zonal convergence and (d)-(f) potential temperature (θ). (g)-(i) As in (d)-(f), but for a shorter, single 34 year period of skeleton model data.

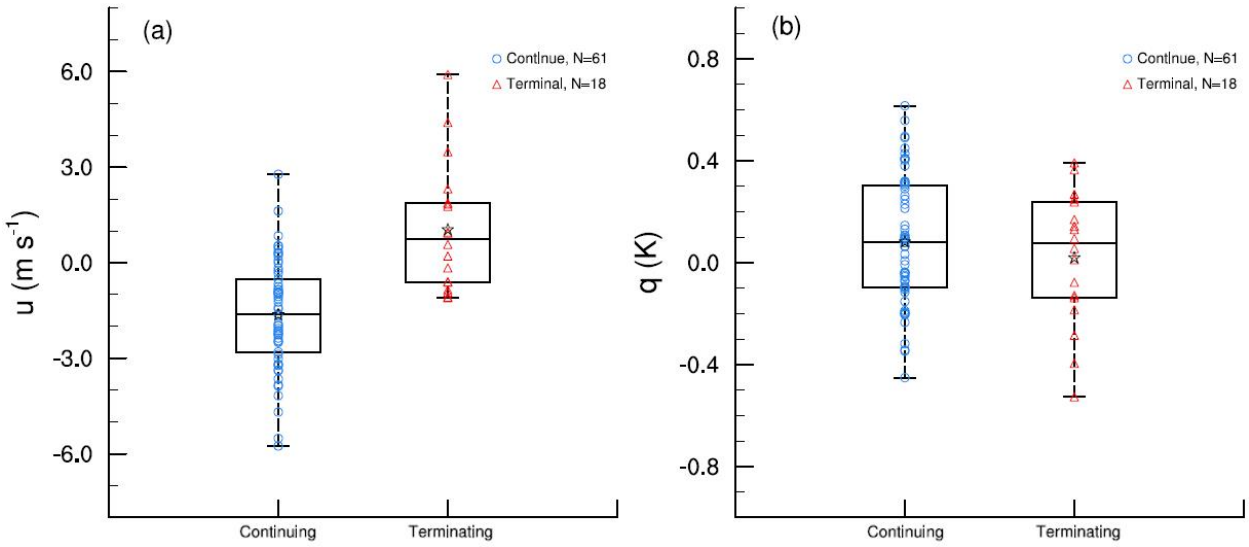

Figure 16. Box-whisker diagrams showing the distribution of (a) zonal wind (*u*) and (b) moisture variable (*q*) anomalies for RMM phase 6 continuing and terminating MJO events averaged over the local domain (120-160°E) at day -10. Box lines indicate the 25%, 50%, and 75% percentiles with whiskers indicating the minimum and maximum values for all events. The blue circles and red triangles represent the local-domain average values for individual continuing and terminating MJO events, respectively. The mean quantities for each event type are overlaid with a black star. All data are taken along the equator and represent 34 years of simulated MJO events using the truncated, observed SSTs (Case-SST8N).